William W. Chadwick, Jr.[1], William S. D. Wilcock[2], Scott L. Nooner[3], Jeff W. Beeson[1,4], Audra M. Sawyer[3], T.-K. Lau[1]

[1] Oregon State University, CIMRS, Hatfield Marine Science Center, Newport, OR, 97365.

[2] School of Oceanography, University of Washington, Seattle, WA, 98195.

[3] University of North Carolina Wilmington, Wilmington, NC, 28403.

[4] NOAA, Pacific Marine Environmental Laboratory, Newport, OR, 97365.

Corresponding author: William W. Chadwick (william.w.chadwick@gmail.com)

Key Points:

- Axial has re-inflated to 85-90% of its pre-2015-eruption level but inflation has slowed and the next eruption still appears to be years away
- The rate of inflation has been highly variable and the last two eruptions appear to be linked to a surge in magma supply that is now waning
- The rates of deformation and seismicity are mutually dependent and evolve with time consistent with a physical model of precursory behavior

AGU Index Terms

8427 Subaqueous volcanism

8416 Mid-oceanic ridge processes

8419 Volcano monitoring

7280 Volcano seismology

8145 Physics of magma and magma bodies

Keywords:

Submarine volcano monitoring, seafloor geodesy, eruption forecasting, bottom pressure recorders, ocean bottom seismometers, OOI cabled observatory

Abstract

Axial Seamount is a basaltic hot spot volcano with a summit caldera at a depth of ~1500 m below sea level, superimposed on the Juan de Fuca spreading ridge, giving it a robust and continuous magma supply. Axial erupted in 1998, 2011, and 2015, and is monitored by a network of instruments including bottom pressure recorders and seismometers. Since its last eruption, Axial has re-inflated to 85-90% of its pre-eruption level. During that time, we have identified eight discrete, short-term deflation events of 1-3 cm over 1-3 weeks that occurred quasi-periodically, about every 4-6 months between August 2016 and May 2019. During each short-term deflation event, the rate of earthquakes dropped abruptly to low levels, and then did not return to higher levels until reinflation had resumed and returned to its previous high. The long-term geodetic monitoring

record suggests that the rate of magma supply has varied by an order of magnitude over decadal time scales. There was a surge in magma supply between 2011-2015, causing those two eruptions to be closely spaced in time and the supply rate has been waning since then. This waning supply has implications for eruption forecasting and the next eruption at Axial still appears to be 5-10 years away. We also show that the number of earthquakes per unit of uplift has increased exponentially with total uplift since the 2015 eruption, a pattern consistent with a physical model that both are caused by increasing differential stress in the shallow crust during magma accumulation.

Plain Language Summary

Axial Seamount is an underwater volcano located offshore Oregon, USA, that is intensely studied because it is frequently active and an ideal site for studying volcanic eruptions, hydrothermal vents, and deep-sea ecosystems. Axial is monitored by a network of seafloor instruments connected to shore by a fiber-optic cable, which is part of the Ocean Observatories Initiative, supported by the National Science Foundation. Monitoring of vertical movements of the seafloor at Axial have shown that it has a repeatable pattern of inflation and deflation that can be used for eruption forecasting. Since its last eruption in 2015, Axial as re-inflated almost to the level of its previous high, but we believe the next eruption is still some years away because the rate of inflation is currently quite low. The monitoring data also show that the rates of earthquakes and uplift are evolving in a predictable way with time, because they are both related to how magma accumulation within the volcano is stressing the overlying crust. Eventually that increasing stress will open a pathway for magma, which will lead to an eruption. This work seeks to understand these processes so that we can better predict the behavior of Axial and other volcanoes.

1. Introduction

Axial Seamount is an active submarine volcano with a summit caldera at ~1500 m depth and a base at ~2400 m, located about 500 km offshore Oregon, USA (Fig. 1). It is a basaltic shield with a magma supply fed by the Cobb hotspot superimposed on the Juan de Fuca spreading ridge (Embley et al., 1990; Chadwick et al., 2005). It has erupted three times in the last 23 years: in 1998, 2011, and 2015 (Embley et al., 1999; Caress et al., 2012; Chadwick et al., 2013; Chadwick et al., 2016; Clague et al., 2017; Clague et al., 2018) and is currently building to its next eruption. It is unique in the world for having the longest record of geodetic monitoring of any submarine volcano, dating back to the early 1980s (Fox, 1990; 1993; Fox, 1999; Chadwick et al., 2006b; Nooner and Chadwick, 2009; Chadwick et al., 2012; Nooner and Chadwick, 2016). This monitoring has been accomplished with various kinds of Bottom Pressure Recorders (BPRs; also known as Absolute Pressure Gauges, or APGs) that can be used as a proxy for depth to monitor vertical movements of the seafloor.

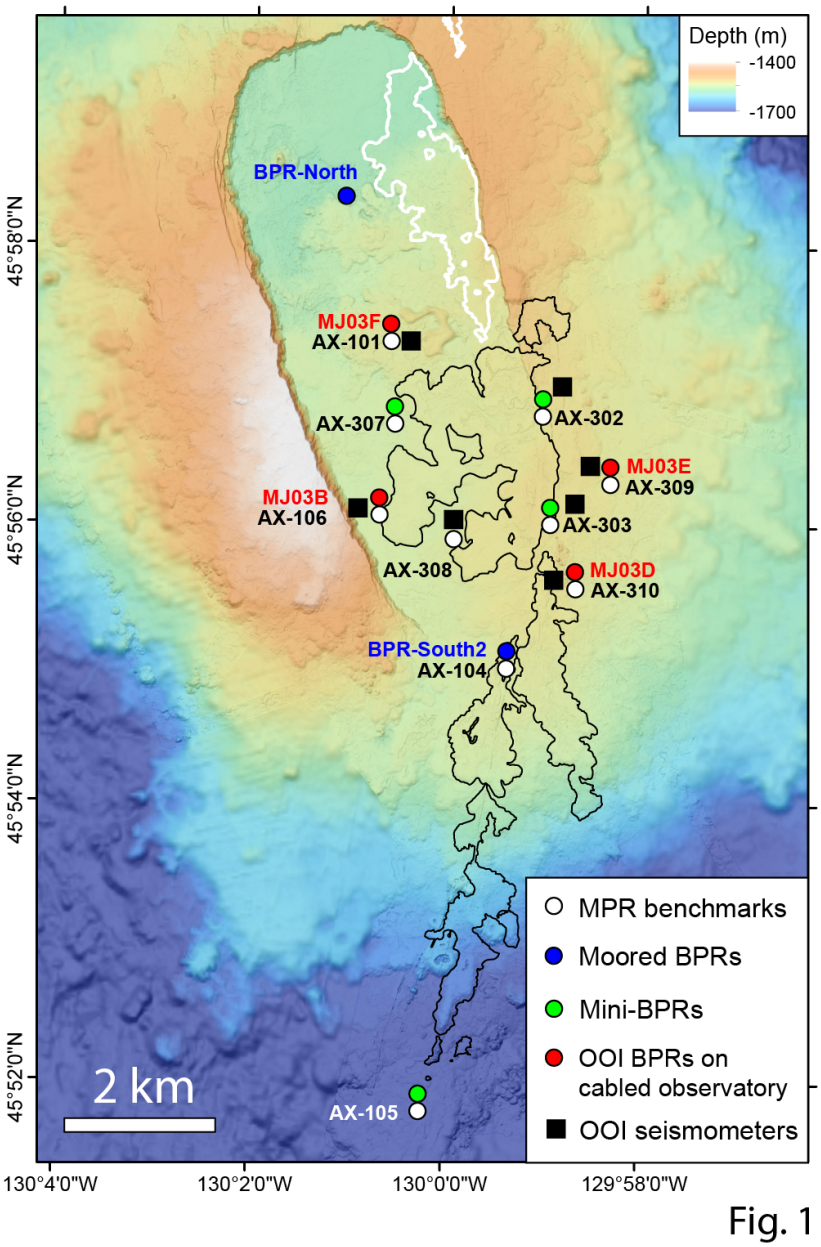

Figure 1. Bathymetric map of the summit caldera of Axial Seamount showing network of Bottom Pressure Recorders (BPR) that were on the seafloor in June 2018 (colored dots). Red dots are BPRs connected to the OOI Cabled Observatory, blue dots are moored-BPRs, and green dots are mini-BPRs deployed on seafloor benchmarks (white dots) where campaign-style MPR measurements are made. *Differential* BPR records are created by subtracting OOI-BPR MJ03E

(Eastern Caldera) from MJ03F (Central Caldera), or by subtracting the mini-BPR record at benchmark AX-105 (the MPR reference station) from the others. Black and white outlines are lava flows erupted in 2011 and 2015, respectively. Black squares are OOI seismometers.

The early years of monitoring at Axial were performed by autonomous, battery-powered BPR instruments that were repeatedly deployed for 1-3 years at the time and then recovered. Since 2000, campaign-style measurements have also been made every few years with a Mobile Pressure Recorder (MPR) at an array of seafloor benchmarks with a remotely operated vehicle (ROV) (Chadwick et al., 2006b; Nooner and Chadwick, 2009; Chadwick et al., 2012). Then in late 2014, the Ocean Observatories Initiative's (OOI) Regional Cabled Array (RCA) came on-line, which provides power and bandwidth to a network of seafloor monitoring instruments at Axial Seamount via a fiber-optic cable connected to shore, including 4 BPR/tilt instruments and 7 seismometers (Kelley et al., 2014). This enables continuous long-term monitoring with real-time data from a diverse set of instrumentation. For example, the cabled observatory was in place during the April 2015 eruption, providing an extraordinary inter-disciplinary dataset that has been used to interpret that event in rich detail (Nooner and Chadwick, 2016; Wilcock et al., 2016; Caplan-Auerbach et al., 2017; Clague et al., 2017; Clague et al., 2018; Levy et al., 2018; Xu et al., 2018; Baillard et al., 2019; Hefner et al., 2020; Le Saout et al., 2020; Waldhauser et al., 2020). Other datasets that provide valuable information on the crustal structure and magma storage system beneath Axial Seamount were collected by a seismic tomography study (West et al., 2001) and two multi-channel seismic reflection surveys, one 2-D survey performed in 2002 (Arnulf et al., 2014; Arnulf et al., 2018) and a 3-D survey in 2019 (Arnulf et al., 2019; Arnulf et al., 2020), which have revealed the location and geometry of a large shallow magma reservoir 1.5-2.5 km below the caldera, and a series of deeper stacked sills from 2.5-4.5 km depth below the southern caldera (Carbotte et al., 2020).

The geodetic monitoring has shown that the pattern of co-eruption deflation and inter-eruption re-inflation at Axial Seamount appears to be fairly repeatable, which was used to successfully forecast the 2015 eruption within a 1-year time window, seven months in advance (Nooner and Chadwick, 2016; Cabaniss et al., 2020). Today, continuous geodetic monitoring at Axial uses a combination of the 4 OOI-BPR/tilt instruments, 4 uncabled autonomous BPR moorings, and 8 additional mini-BPRs that are deployed and recovered by an ROV on the MPR benchmarks, in addition to the campaign-style MPR measurements every 2 years. In addition, repeated bathymetric surveys by autonomous underwater vehicles (AUVs) have been used since 2011 to detect depth changes at lower resolution but over a larger area (Caress et al., 2015; Caress et al., 2016; Nooner et al., 2017; Caress et al., 2020).

Here, we present BPR time-series data during the re-inflation of the volcano since its 2015 eruption, focusing mainly on its temporal evolution and its relation to seismicity. The BPR data show a slowing rate of inflation with time, and

superimposed on that we identify 8 repeated short-term deflation events between 2016-2019 that were co-incident with a sharp reduction in the rate of seismicity (Natalie et al., 2018). The decrease in inflation rate reflects changes in the magma supply to the volcano, which in turn have implications for eruption forecasting. Finally, we show that the deformation and seismicity are tightly linked and evolving with time as predicted by a physical model of the changing proportion of elastic and inelastic deformation as the crust is being stressed during inter-eruption magma accumulation.

2. Methods

The continuously-recording BPRs that we have used at Axial Seamount use pressure sensors made by Paroscientific, Inc., and make a recording every 15 or 100 sec in the uncabled instruments, and at a rate of 20 Hz in the cabled instruments. The pressure data are first converted to equivalent depth and are de-tided. There are two possible methods for removing the tides – one can either subtract a predicted tide model, or low-pass filter the data to remove tidal frequencies, and each method has its pros and cons. Subtracting predicted tides retains high-frequency information in the records, but does not completely remove the tidal signal (leaving some residuals), whereas the filtering option removes all of the tidal signal, but can also remove some high-frequency geodetic signals that may be of interest. At Axial, we choose to subtract a predicted tide model, because we want to retain high-frequency information that may be geophysical in origin. The remaining signal has several non-geophysical sources of noise that have to be accounted for: instrumental drift (up to ~20 cm/yr) (Polster et al., 2009), tidal residuals of ±5 cm at tidal frequencies, and non-tidal oceanographic signals (due to winds, atmospheric pressure changes, ocean circulation, etc) of ±5 cm at longer periods of days to weeks (Inazu et al., 2012; Dobashi and Inazu, 2021).

Drift is not a significant problem for detecting short-term events (over days), such as co-eruption deflation, but it is a major concern for measuring long-term inflation, because drift can be of the same magnitude. To address the drift issue, we have used the ROV-based MPR measurements to make surveys at an array of 10 seafloor benchmarks every 1-3 years, by using one benchmark located 10 km south of the center of the caldera as a reference site (AX-105 in Fig. 1, assumed to be stable) and computing the relative depths of the other benchmarks in or near the caldera with a repeatability of ~± 1 cm (Chadwick et al., 2006b; Nooner and Chadwick, 2009; Chadwick et al., 2012; Nooner and Chadwick, 2016). The MPR measurements can also constrain the drift of any BPRs that are co-located at the benchmarks. For example, the MPR data from 2015-2020 have shown that the OOI BPRs all happen to have negligible drift rates (< 0.5 cm/yr). All the BPR data presented in this paper are either drift-corrected or did not need correcting. Other more recent approaches to quantifying BPR drift use modified sensors with a known reference pressure to compare with the ambient pressure over time (Sasagawa et al., 2016; Cook et al., 2019; Manalang et al., 2019; Wilcock et al., 2021), some of which are being

tested at Axial, but we do not employ these methods here.

The de-tided and drift-corrected BPR data are still overprinted with tidal residuals and non-tidal oceanographic noise. In other settings, two approaches have been used to remove the latter by either subtracting a global ocean model (Inazu et al., 2012; Muramoto et al., 2019; Dobashi and Inazu, 2021) or by subtracting the record of a nearby BPR that is outside the zone of deformation but experiences nearly the same oceanographic noise (Wallace et al., 2016; Fredrickson et al., 2019). For the BPR data from Axial, we have chosen to subtract data from a reference BPR in one of two ways. For the OOI cabled BPR data, we subtract data from the BPR with the smallest deformation signal (MJ03E) located on the east rim of the caldera, from the BPR with the largest deformation signal (MJ03F) located at the center of the caldera (Figs. 1 & 2). For non-cabled BPR data recorded on the MPR benchmarks, we use data from benchmark AX-105 as a reference (Fig. 1). In either case, this has the desired effect of removing most of the tidal residuals and the non-tidal oceanographic signals that are common to both instruments, since they are located at similar depths only a few km apart. This reduces the noise level from ± 5 to ± 1 cm and yields a *differential* BPR record that is a much clearer representation of the geophysical signal in which we are interested (Fig. 2). Throughout the rest of this paper, we will differentiate between *differential* BPR data, and data from a *single-station* BPR. Both are valuable since the *single-station* BPR data provide information on seafloor deformation at specific sites that can be modeled or used to calculate magma supply rates, whereas the *differential* BPR data provide a clearer view of temporal trends and changes in uplift rates. Note, however, that a *differential* BPR record is not the same as uplift or subsidence of the seafloor at a single-station; rather it is the *difference* in uplift or subsidence at one station relative to another. Experience has shown that the MJ03F-MJ03E *differential* BPR uplift (the caldera center relative to the eastern caldera reference) is about 60% of the *single-station* uplift measured at the caldera center BPR. Near-real-time data from *single-station* OOI BPRs, and the MJ03F-MJ03E *differential* BPR time-series, are displayed at this web site: https://www.pmel.noaa.gov/eoi/rsn/

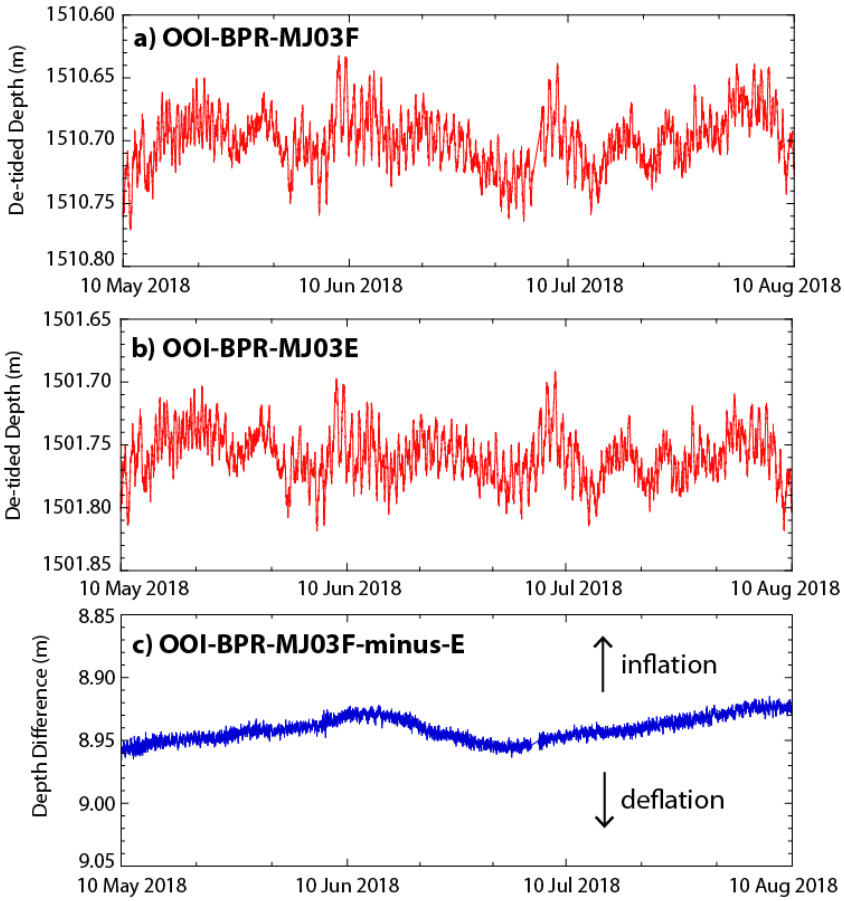

Fig. 2

Figure 2. Comparison of de-tided *single-station* BPR data to *differential* BPR data. (a) Three months of de-tided data from OOI-BPR-MJ03F at the Central Caldera, overprinted with higher-frequency tidal residuals and lower-frequency non-tidal oceanographic noise. (b) De-tided data from OOI-BPR-MJ03E at the Eastern Caldera over the same time period, showing a similar pattern of noise. (c) *Differential* BPR record over the same time period, created by subtracting (b) from (a), which removes the common sources of noise and makes the geodetic signal much clearer. All 3 plots have the same scale on the y-axis (20 cm). The OOI-BPRs at MJ03F and MJ03E consistently have the largest and smallest vertical movements, respectively, so their differential record shows the uplift of MJ03F relative to MJ03E. Locations of BPRs are shown in Figure 1.

Below, we compare the BPR data since the 2015 eruption to the temporal and spatial variations of earthquakes at Axial Seamount to gain insight into the

magma supply and storage system. The seismic data from the OOI seismometers are processed automatically to yield histograms of the number of earthquakes with time and maps of their epicenters (Wilcock et al., 2016; Wilcock et al., 2017; Wilcock et al., 2018). A near-real-time catalog of the earthquake detections at Axial Seamount is available at this web site: http://axial.ocean.washington.edu/

3. Results

Figure 3 is a long-term plot of the *single-station* BPR record of inflation and deflation at the center of Axial caldera. The plot shows co-eruption deflation of 2.5 to 3.2 m during the three eruptions, and inter-eruption re-inflation at a rate that has varied significantly with time (10-100 cm/yr). It also shows that the deformation cycle is fairly repeatable, but not exact. For example, the inflation threshold reached before the 2015 eruption was 30 cm higher than the one reached in 2011. Also, the exact relationship between the 1998 and 2011 inflation thresholds is unknown because of the data gap between 1998-2000, but nevertheless this pattern can be used as a basis for forecasting the timing of future eruptions (Nooner and Chadwick, 2016; Cabaniss et al., 2020).

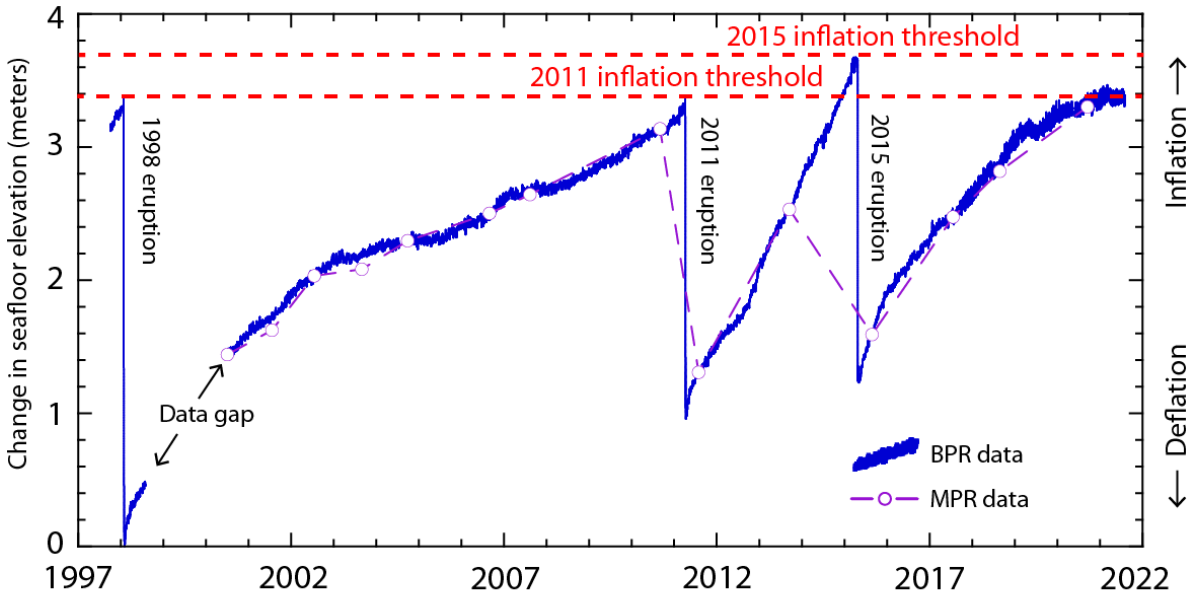

Fig. 3

Figure 3. Long-term *single-station* BPR record from the Central Caldera (near MJ03F and AX-101 in Figure 1) showing vertical movements of the seafloor over time. The blue curve is BPR data from multiple non-cabled instruments before 2017 and from OOI-BPR MJ03F since 2017. Purple dots are MPR data used to tie multiple records together and to remove drift from the BPR data. Note that

the relative displacement across the data gap between 1998-2000 is unknown. Plot shows the major short-term deflation during eruptions in 1998, 2011, and 2015 and long-term re-inflation between eruptions at variable rates. The overall deformation cycle appears to be inflation-predictable, which can be used to forecast eruptions.

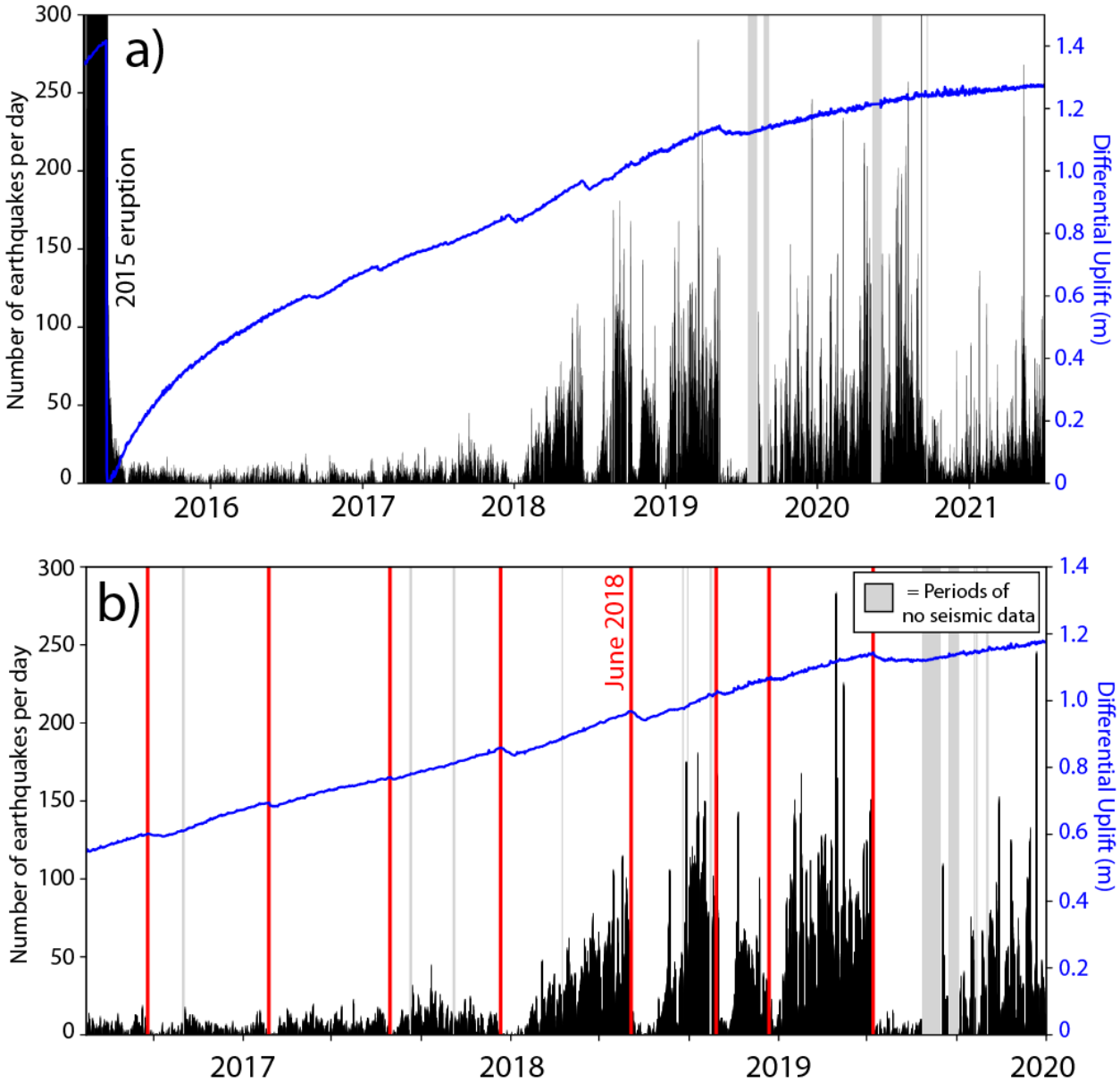

Fig. 4

Figure 4. Plots of *differential* OOI-BPR data (blue curves) over histograms of the number of earthquakes per day (black bars) showing how deformation and seismicity have co-varied. (a) All data since the 2015 eruption. (b) Data

between mid-2016 to 2020, with the start times of the eight identified short-term deflation events shown by vertical red lines (June 2018 event, shown in more detail in Figure 5, is labeled). Grey vertical stripes show times when no seismic data are available from the Wilcock et al. (2017) catalog (including 3-week period of a multi-channel seismic survey in August 2019). Differential BPR data are uncorrected.

We know from previous studies of the seismicity at Axial over multiple eruption cycles that the number of earthquakes is very low immediately after an eruption for months to years, and then it gradually increases with time leading up to the next eruption (Dziak and Fox, 1999; Sohn et al., 1999; Sohn et al., 2004; Dziak et al., 2012; Wilcock et al., 2016; Wilcock et al., 2018). This has also been the case since the 2015 eruption. For example, the peak number of earthquakes detected by the OOI seismic network during the final 4 months before the 2015 eruption increased from several hundred per day, to a thousand per day, to several thousand per day (Wilcock et al., 2016). Then after the eruption the rate of seismicity quickly fell to only about 10 earthquakes per day. Multiple studies have also shown that most earthquakes at Axial occur along outwardly dipping faults beneath the eastern and western sides of the caldera, with the vast majority under the eastern caldera rim (Wilcock et al., 2016; Wilcock et al., 2018). The outwardly-dipping faults are located between the shallow magma reservoir and the surface, but do not reach the seafloor. Remarkably, these faults are active during both inflation and deflation and reverse their sense of slip (Levy et al., 2018). Careful earthquake relocations with a refined velocity model show some evidence that a smaller number of earthquakes on the eastern side of the caldera may be located on the inwardly-dipping caldera fault that reaches the surface and defines the caldera rim (Arnulf et al., 2018; Baillard et al., 2019; Waldhauser et al., 2020), but slip on these faults may largely be aseismic. The overall geometry of the inwardly-dipping and outwardly-dipping faults follows orientations predicted by analog experiments of caldera collapse (Roche et al., 2000).

Figure 4a compares the record of re-inflation to the seismicity observed since the 2015 eruption. The blue curve is the *differential* BPR record and the black histogram shows the number of earthquakes detected per day. The plot shows that the seismicity at Axial remained at a very low level (~10 per day) for several years, despite a relatively high rate of re-inflation right after the eruption (>100 cm/yr). Then in 2017 or early-2018, the rate of seismicity began to gradually increase, after the volcano had recovered ~60% of the subsidence that occurred during the 2015 eruption. The rate of seismicity rose up to peaks of a few hundred events per day by mid-2019, but has been quite variable since then (Fig. 4a).

The plot also shows that there have been several brief reversals in the differential re-inflation curve, which we refer to as "short-term deflation events" and examine in more detail below. We've identified eight of these events from mid-2016 to mid-2019 (Fig. 4b and Table 1), when they were quasi-periodic, occurring

about every 4-6 months. During each short-term deflation event, there was 1-3 cm of deflation over 1-3 weeks. Also during each deflation event, the level of seismicity dropped back to low levels for about a month, which is most obvious in the later deflation events when overall seismicity rates were higher.

We can see the close linkage between deformation and seismicity more clearly by zooming into individual short-term deflation events. Figure 5a shows a plot of the differential BPR data over 3 months during the June 2018 deflation event, and Figure 5b is a histogram of earthquakes per day over the same time period. In the differential BPR plot, the deflation amounts to 2.7 cm over 18 days. The histogram of earthquakes shows that as soon as deflation started, the number of earthquakes dropped to low levels and the seismicity remained low until the volcano had re-inflated to the level it was at when the short-term deflation event began. All the other short-term deflation events display a similar pattern (see Supporting Information), except the last one in May 2019. Figures 5c and 5d show differential BPR data and a histogram of seismicity for the May 2019 deflation event (2.4 cm of deflation over 16 days), which was slightly different in that it was followed by 2 months of no inflation in the differential BPR record while the level of seismicity remained low. Then when re-inflation resumed it was at a distinctly slower rate than before the event.

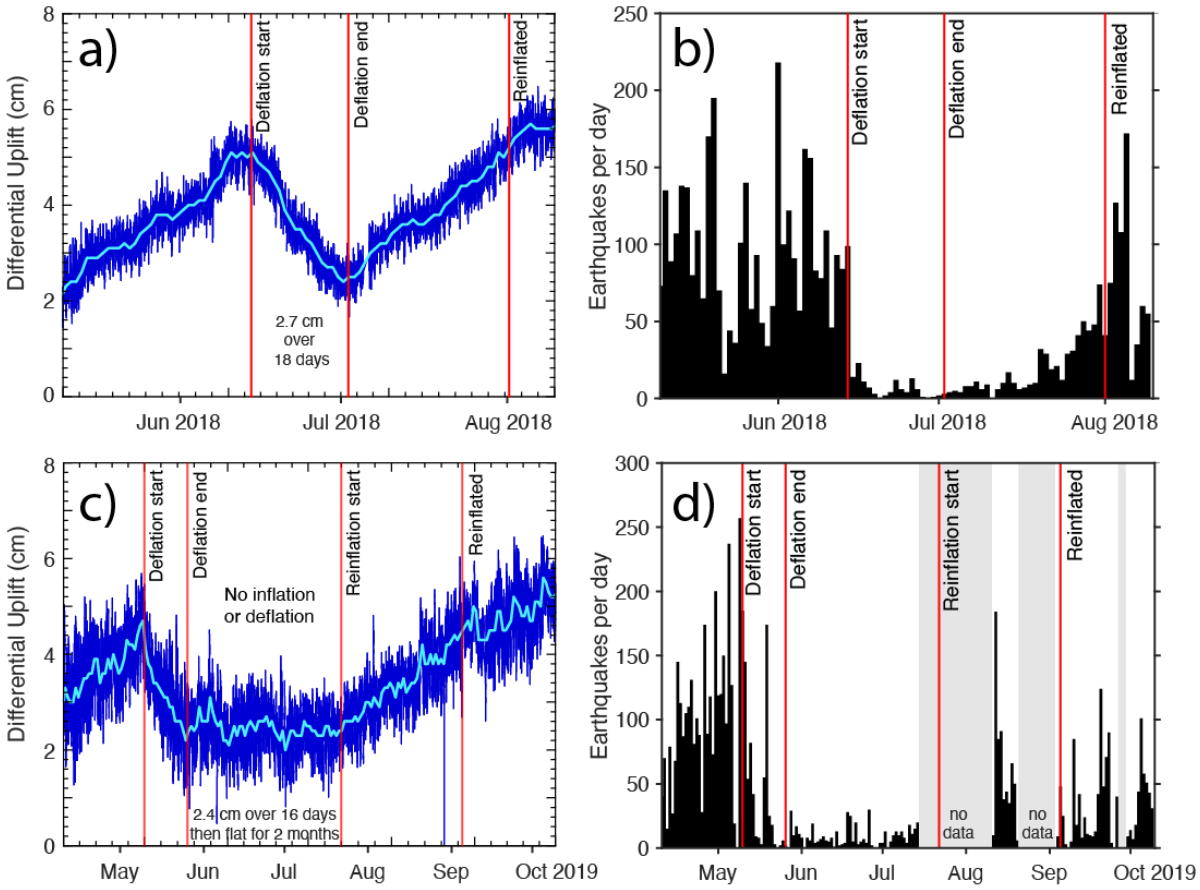

Fig. 5

Figure 5. Deformation and seismic data during the June 2018 and May 2019 short-term deflation events. (a) Uncorrected differential BPR data over 3 months from 10 May to 10 August 2018. Dark-blue curve is data sub-sampled to every 15 minutes; light-blue curve is data averaged over 1-day windows. Vertical red lines show the times when deflation started, ended, and when re-inflation reached the previous level. (b) Histogram of the number of earthquakes per day over the same time interval as in (a). Comparing the two plots shows that the seismicity sharply decreased during the short-term deflation event and did not resume until re-inflation reached the previous level. (c) Uncorrected differential BPR data over 6 months from 10 April to 10 October in 2019. (d) Histogram of earthquakes during same time period as in (c). Grey bars show periods when seismic data are unavailable. Note period of 2 months following the end of the

May 2019 deflation event with no inflation or deflation when seismicity remained low. Similar records for the other short-term deflation events are provided in the Supporting Information.

4. Discussion

4.1. Possible causes of the short-term deflation events

Looking at the deformation and seismicity together shows that they are tightly linked, but what might be happening during the short-term deflation events to explain these observations? The multichannel-seismic reflection data show that the magma storage system at Axial Seamount consists of a shallow magma reservoir about 1.5-2.5 km beneath the seafloor, underlain by a series of stacked sills that apparently feed magma upward (Arnulf et al., 2014; Arnulf et al., 2018; Carbotte et al., 2020). Specifically, Carbotte et al. (2020) infer that melt ascends through the stacked sills by porous flow and that the melt-rich layers form by mush compaction in a viscoelastic matrix. Building on the conceptual model developed by Nooner and Chadwick (2009), Figure 6a depicts an interpretive cross-section in which inter-eruption inflation is occurring as magma is supplied upward through the sill complex to the shallow magma reservoir. This increases the pressure in the shallow reservoir and the stress in the overlying crust, which causes inflation, and in turn generates earthquakes on the caldera-related faults.

One hypothesis for the short-term deflation events is that they could be caused by magma moving laterally out of the shallow magma reservoir beneath the caldera, either into one of the rift zones or perhaps into a satellite reservoir (Fig. 6b) such as the one imaged seismically ~8 km to the east of the caldera (Arnulf et al., 2014; Arnulf et al., 2018), which causes deflation in the caldera, reduces the pressure in the main reservoir, and effectively turns off the earthquakes. If this were happening we might see some evidence of where the magma was moving. There would presumably be inflation occurring somewhere outside the caldera leading to shallowing depth and possibly some earthquakes along the magma path or surrounding the satellite reservoir (Fig. 6b).

Sawyer et al. (2019; 2020) examined data recorded by 10 non-cabled mini-BPR instruments throughout the caldera during the June 2018 short-term deflation event, using the BPR record from the southern-most MPR benchmark (AX-105) as a reference to create *differential* BPR records that better isolate the geodetic signal (Fig. 7). These data show that all the BPRs recorded subsidence during the short-term deflation event, confirming that its spatial extent covered the entire caldera (Fig. 1). They modeled the subsidence observed during the deflation event and found that the best-fit solution was similar to the model of Hefner et al. (2020), a steeply dipping prolate spheroid located inside the SW rim of the caldera (Fig. 7); the Hefner model was based on the much larger co-eruption deflation measured between 2013-2015, but also fits other inflationary periods. This shows that the deformation source during the June 2018 short-term deflation event was located within the caldera and was similar to that observed at other times (during both inflation and deflation), suggesting that the deflation

events are not simply minor redistributions of magma within the subcaldera reservoir. There is no evidence for inflation occurring outside the caldera during the short-term deflation events, although we have few observations there and none over the eastern satellite body.

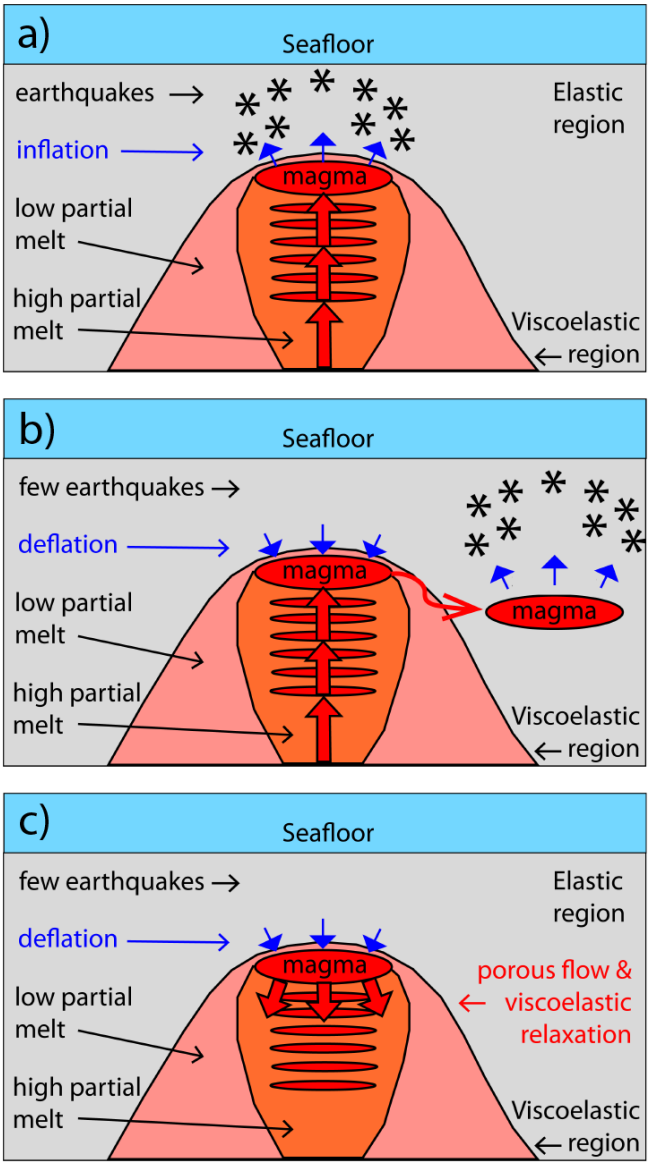

Fig. 6

Figure 6. Cartoon illustrating two possible hypotheses to explain the short-

term deflation events at Axial Seamount. (a) Idealized cross-section showing shallow magma reservoir and underlying stacked sills within a viscoelastic region of partial melt (modified from Nooner and Chadwick (2009), and based on results from Arnulf et al. (2018), and Carbotte et al. (2020)). During re-inflation, magma is supplied upward through the stacked sills to the shallow reservoir, where increasing pressure causes uplift (elastic deformation) and earthquakes (inelastic deformation) in the overlying crust. (b) One hypothesis for the short-term deflation events is that magma is transferred laterally to a satellite reservoir, which would cause deflation and a reduction in seismicity in the caldera, but might be expected to cause uplift and increased seismicity elsewhere. (c) An alternative hypothesis is that the deep supply of magma is temporarily interrupted and the deflation is due to viscoelastic relaxation and porous flow out of the shallow magma reservoir into its surroundings. See text for discussion.

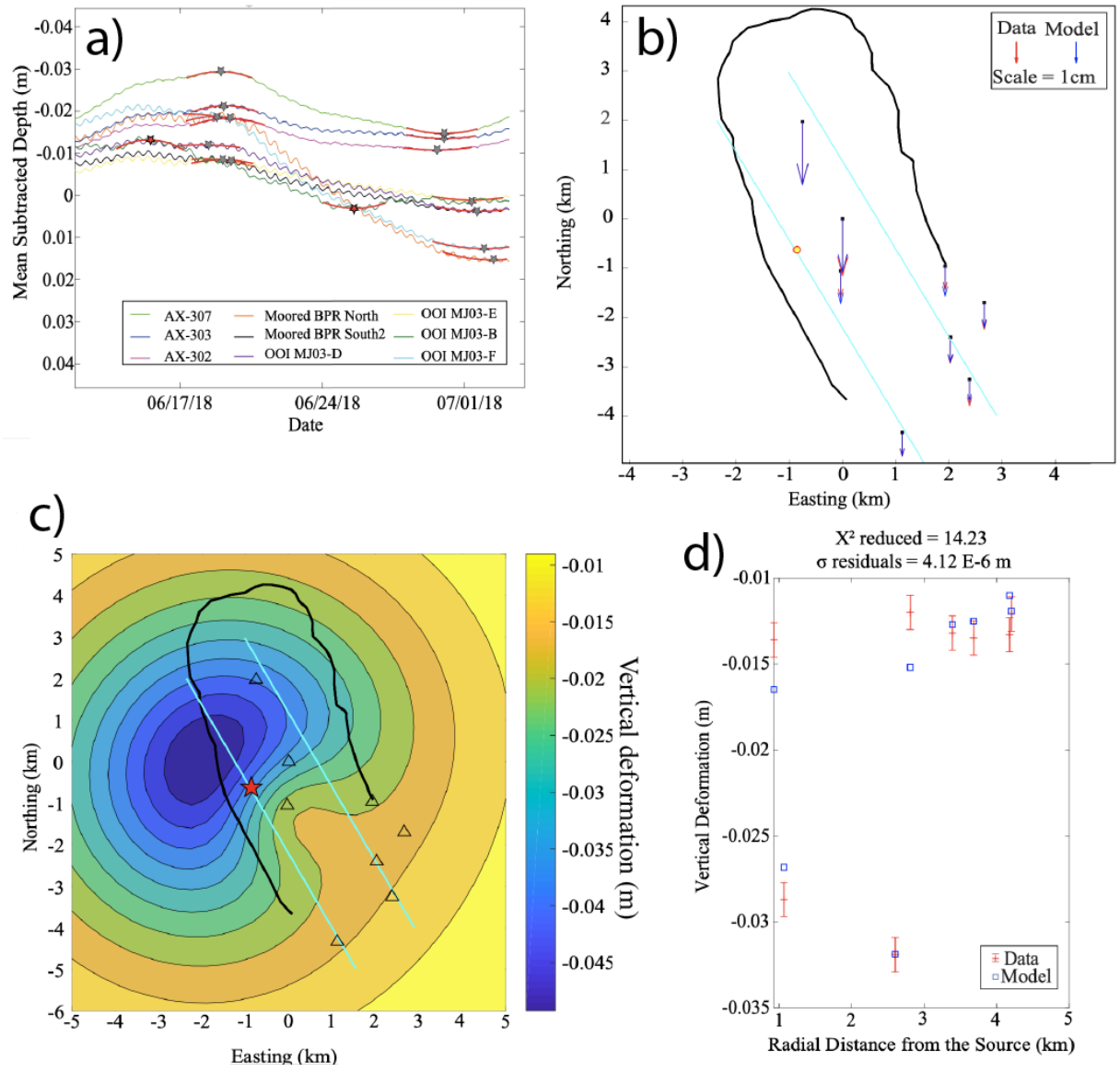

Fig. 7

Figure 7. *Differential* BPR records from 9 sites during the June 2018 short-term deflation event, created using the data from the mini-BPR at benchmark AX-105 as a reference (see Figure 1 for locations). (a) Each BPR record has

had a mean depth subtracted so they can be plotted together, but are otherwise uncorrected. Red lines and stars show start and end of short-term deflation event in each record. (b) Comparison of best-fit deformation model (in blue) with data (in red) in map view (black line is caldera outline; yellow dot is model centroid; light-blue lines are model faults as in Hefner et al. (2020)). (c) Map view of predicted subsidence from best-fit deformation model (colors), which is similar to the best-fit model of Hefner et al. (2020). (d) Comparison of best-fit model (in blue) and data (in red) in plot of vertical displacement vs. radial distance from source. Figures from Sawyer et al. (2019).

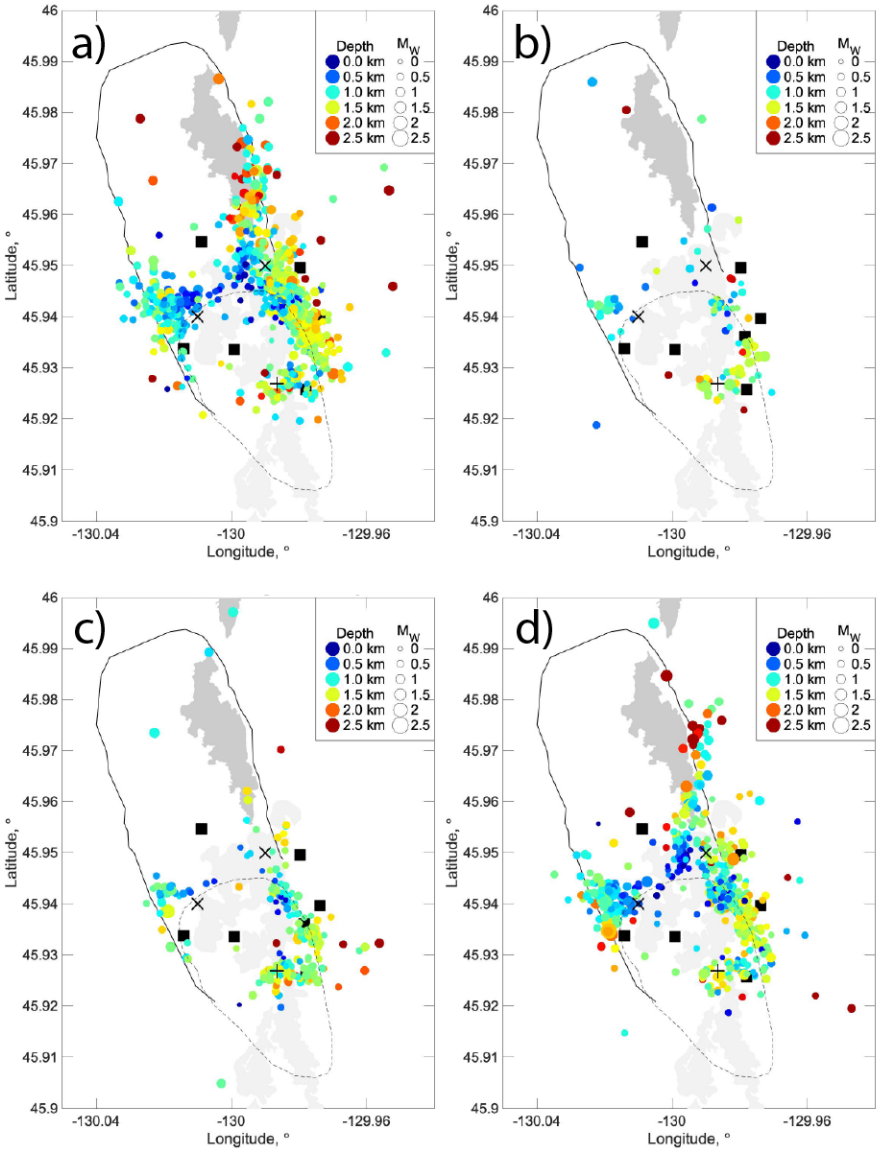

Fig. 8

Figure 8. Maps of earthquake epicenters detected before, during, and after the June 2018 short-term deflation event, color-coded by depth (see legend), showing that the spatial pattern of seismicity did not change during the event. (a) Earthquakes from the 24 days before the deflation event (21 May-14 June). (b) Earthquakes from the 18 days during the deflation event (14 June-02 July). Earthquakes during the next 30 days of re-inflation (02 July-01 August). (d)

Earthquakes during the next 24 days after the level of re-inflation had returned to its previous high and higher seismicity resumed (01-25 August). Arcuate outline is caldera rim, dashed outline is deep stacked sills from Carbotte et al. (2020), "+" symbol is approximate center of sills, X's are centroids of best-fit deformation models of Nooner and Chadwick (2016) at right and Hefner et al. (2020) at left, black squares are OOI seismometer locations, light- and dark-grey areas are lava flows erupted in 2011 and 2015, respectively. Similar maps for the other short-term deflation events are provided in the Supporting Information.

The spatial pattern of seismicity does not change markedly during the short-term deflation events. Figure 8a is a map of earthquake epicenters from the catalog of Wilcock et al. (2017) during the 3 weeks before the June 2018 deflation event, and Figure 8b is a similar map during the following 3-weeks of deflation. Comparing the two shows that the seismicity is in essentially the same pattern, but there are just fewer earthquakes during the short-term deflation event. Similarly, Figure 8c shows the earthquakes during the following month after the deflation event had ended and the volcano was re-inflating to the previous level, while the seismicity was still low, and Figure 8d shows the pattern of earthquakes after the volcano had re-inflated beyond that previous level and a higher level of seismicity had resumed. Again, the spatial distribution of earthquakes is similar during the two time periods. The pattern of seismicity during the other short-term deflation events is similar (see Supporting Information). These observations do not support or refute the hypothesis of lateral magma movement out of the subcaldera reservoir, but require that it occurs aseismically if it is happening.

An alternative hypothesis is that the supply of magma to the shallow reservoir is temporarily interrupted during these short-term deflation events (Fig. 6c). During the time that the supply stops, the viscoelastic region surrounding the reservoir relaxes, outwardly directed porous flow from the shallow reservoir reduces its internal pressure, which leads to deflation and a drop in the stresses driving the seismicity. This idea perhaps seems more likely during a period when the rate of inflation (and magma supply) are decreasing, whereas the first hypothesis might be more likely during a period of increasing inflation and magma supply rate. However, the observed rate of subsidence during the short-term deflation events (~50 cm/yr) seems higher than one might expect for a viscoelastic relaxation mechanism, and it does not appear to decrease exponentially which also might be expected. Therefore, we do not have enough clear evidence to favor one hypothesis over the other, and conclude that more observational data and perhaps viscoelastic modeling is needed to resolve this question.

4.2. The May 2019 short-term deflation event and changes in inflation rate

As mentioned above, the May 2019 short-term deflation event was similar to the others, but was also different in that it was followed by 2 months of no inflation while the seismicity remained low (Figs. 5c & d). This time period with neither inflation nor deflation could be interpreted as either a period of no magma supply, or a period when the magma supply had resumed but at such

a low rate that it only approximately counterbalanced the rate of viscoelastic relaxation or the porous flow of magma from the reservoir into the surrounding crystal mush. In any case, the May 2019 event also marked a distinct decrease in the long-term rate of inflation. This is shown in Figure 9 which shows the average rate of corrected *differential* uplift calculated for each interval between the 8 short-term deflation events, and also for two (somewhat arbitrary) time periods before and after them. The *differential* rates of uplift in Figure 9 have been corrected to approximate the *single-station* rate of uplift at the caldera center by multiplying by 1.67. A case can be made that the average rate of uplift also changed to a lesser extent between some of the other short-term deflation events. Another major decrease in uplift rate occurred around August-September 2020 when there was no obvious deflation event but there was a distinct decrease in the rate of seismicity (Fig. 4a). Figure 9 shows that after the 2015 eruption, between May 2015 and January 2016, the rate of re-inflation was relatively high, and average of 103 cm/yr, but already decreasing. The rate continued to decrease between January 2016 and May 2019, when the average rate was between 35-55 cm/yr. Then after May 2019, the rate decreased further by about half to 19 cm/yr, and then it decreased by more than half again to only 7 cm/yr between August 2020 and the time of this writing in August 2021.

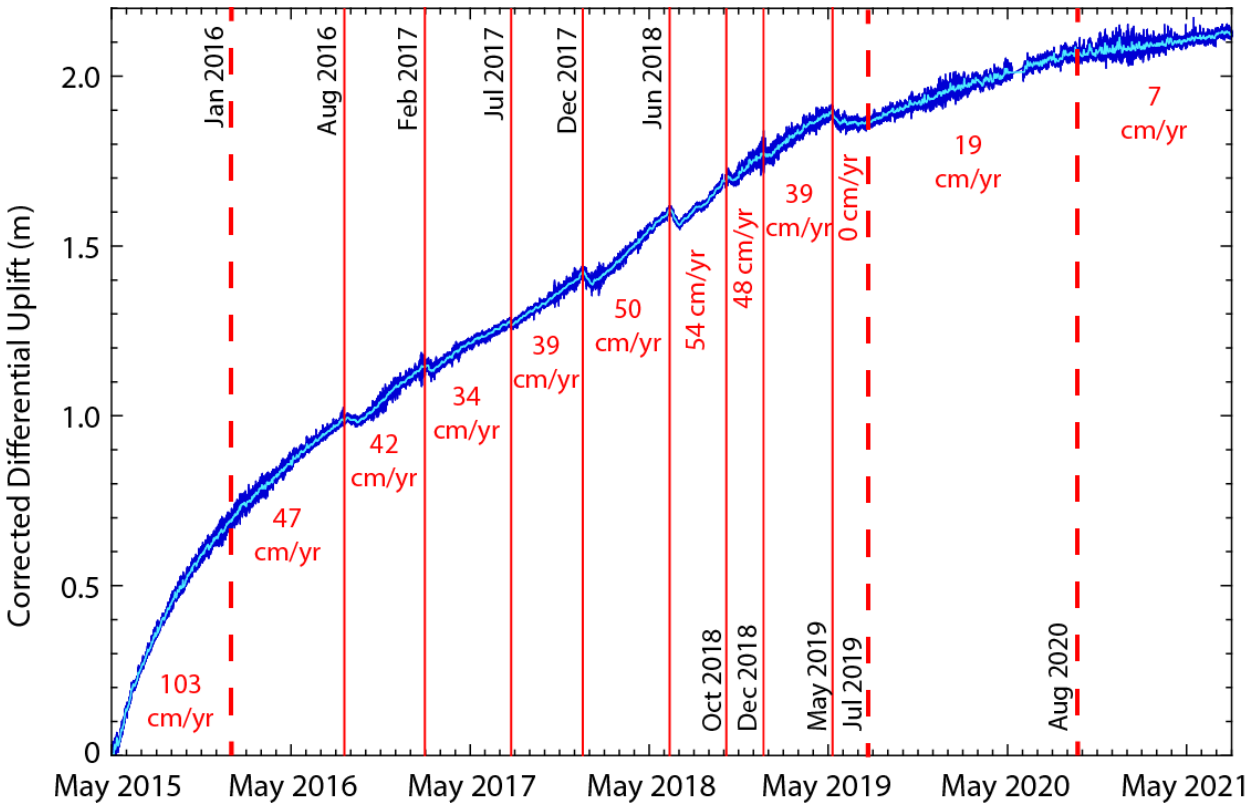

Fig. 9

Figure 9. Plot of *differential* BPR data (OOI-BPR-MJ03F-E) from the 2015 eruption to the present, corrected to approximate uplift at the *single-station* uplift at the caldera center by multiplying by 1.67. Dark-blue curve is data sub-sampled to every 15 minutes; light-blue curve is data averaged over 1-day windows. Overlain in red are average rates of uplift between each of the short-term deflation events (vertical red lines), and between other somewhat arbitrary times of apparent rate changes (vertical dashed lines). Note minor changes in rates between some short-term deflation events and major changes in rates in May 2019 and around August 2020.

We interpret that the decreasing rate of uplift reflects a sharply waning magma supply, and the short-term deflation events observed between 2016-2020 may be a consequence of this waning supply. Perhaps when the driving pressure that feeds magma upward through the stacked sills to the shallow reservoir wanes, it can be temporarily insufficient to keep the conduits open that transport magma upwards, such that they close until the driving pressure builds again to re-open them and a new equilibrium supply rate is re-established. This idea

is more consistent with the second of the hypotheses presented in Section 4.1 above. If true, this re-equilibration process occurred repeatedly during the time period when the deflation events were occurring and the magma supply rate was waning.

Since May 2019, after re-inflation resumed and the inflation rate decreased by half, we have not identified any other obvious short-term deflation events in the differential BPR record (Figs. 4a & 9). Why did they stop? Perhaps the magma supply rate had stabilized at a new lower level and so the temporary interruptions associated with the decreasing rate of supply stopped. Another question is whether any short-term deflation events were observed before 2015. None are obvious, but this could be because we did not have the capability to create an effective differential BPR record before 2014 when the OOI-RCA was deployed, because all the non-cabled BPRs were located too close to one another to provide an adequate reference (their rates of inflation were not different enough from each other).

4.3. The long-term inflation record and changes in magma supply with time

Another way of examining how the long-term rate of uplift has changed with time is by using the continuous BPR record at the center of the caldera and calculating daily average rates using a sliding time window of various widths. We have done this in Figure 10, using both the corrected *differential* BPR record since 2014, and the *single-station* BPR record extending back to 1997. Figure 10a shows the variation in the uplift rate since the 2015 eruption, calculated from the corrected *differential* BPR record, averaged over time windows of 1 month, 3 months, 6 months, and 1 year. Overall, it is clear that the rate of uplift has been decreasing sharply since the 2015 eruption. The arrows in Figure 10a show the 8 identified short-term deflation events, which are visible as dips in the uplift rate in the 1-month average curve. The 1-year average curve shows longer-term trends, including a rapid decrease in uplift rate in the first 2 years after the 2015 eruption, followed by 2 years of a relatively steady rate until May 2019, when the rate suddenly decreased and it has been on a downward trend since then. Figure 10b compares the uplift rate calculated using the corrected *differential* BPR record vs. the *single-station* BPR data, both averaged over a 1-year moving time window, showing good agreement between the two. This confirms that our correction factor for the *differential* rates is valid and enables comparison of rates derived from the longer *single-station* BPR record. In Figure 10b, we speculate that the apparently higher uplift rates in the fall/winter of each year in the *single-station* curve may be seasonal oceanographic effects that are removed from the *differential* record.

Figure 10c shows the longer-term variation in uplift rate from 1997-2022, derived from the *single-station* BPR record, again averaged over a 1-year moving time window (blue curve). Of course, the rates would be higher if averaged over a shorter time window. For example, the large co-eruption deflations (which only last 1-4 weeks) effectively drown out higher rates of inflation both before and after eruptions with a 1-year averaging window. Nevertheless, Figure 10c shows

that the 1-year averaged uplift rate has varied from <10 to >80 cm/yr since 1997, with the highest rates between the 2011 and 2015 eruptions.

We can calculate the average magma supply rate (red curve in Figure 10c), based on the best-fit deformation model of Nooner and Chadwick (2016), which implies that there is 1.3 x 10^6 m^3 of magma added to the shallow reservoir for every 1 cm of uplift (see Supporting Information; the numbers would be similar if we used the Hefner et al. (2020) model instead). While these supply rates are highly dependent on the deformation model, they provide a quantitative illustration of how much the magma supply has changed with time. In Figure 10c the magma supply rates are relatively high after the 1998 eruption (30-60 x 10^6 m^3/yr), they decreased until they reached a low in 2005 (<10 x 10^6 m^3/yr), then they gradually increased again leading up to the 2011 eruption (20-30 x 10^6 m^3/yr). After the 2011 eruption, the rates were suddenly substantially higher (55-100 x 10^6 m^3/yr) and even increased leading up to the 2015 eruption. Since then, the rates have decreased rapidly as discussed above.

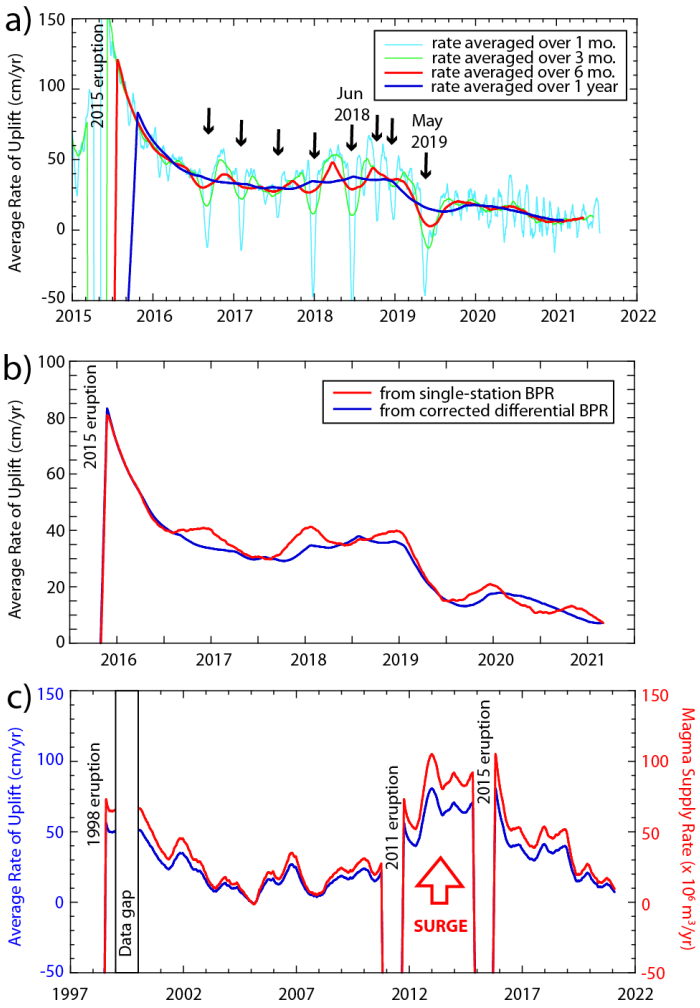

Fig. 10

Figure 10. Variation of average rate of uplift at the caldera center and magma supply rate over time. (a) Plot showing variation in uplift rate since the 2015 eruption, derived from the differential BPR record (OOI-BPR-MJ03F-E), averaged over different time periods (1 month in light-blue, 3 months in light-green, 6 months in red, and 1 year in blue). Differential BPR data are corrected to approximate the single-station uplift at the caldera center by multiplying by 1.67. Arrows show the 8 identified short-term deflation events visible as dips in the uplift rate in the 1-month average curve (light-blue). (b) Plot comparing uplift rate averaged over a 1 year time window using the corrected differential BPR record (in blue) to the single-station BPR data (in red), showing good agreement. (c) Long-term plot showing variation in uplift rate from 1997-2022,

derived from the single-station BPR record at the center of the caldera, averaged over a 1-year moving time window (blue curve, left y-axis) and magma supply rate calculated from the averaged uplift rate and the best-fit deformation model of Nooner and Chadwick (2016) (red curve, right y-axis). A surge in the magma supply occurred between the 2011-2015 eruptions.

Looking at this long-term view, it becomes clear that there was a surge in the magma supply rate to Axial between the 2011 and 2015 eruptions. This would explain why those two eruptions were so close together in time (Chadwick et al., 2016), and shows that the eruption recurrence interval at Axial depends strongly on the underlying rate of magma supply (Nooner and Chadwick, 2016). Figure 10c also shows that the recent decrease in rates is similar to the post-1998 eruption time period. The overall long-term pattern approximates a sinusoidal curve of decreasing and increasing rates with a wavelength of about a decade, and a magma supply amplitude that varies by about an order of magnitude (from <10 x 10^6 m^3/yr to >100 x 10^6 m^3/yr). Continued monitoring will show if this pattern continues and if the current relatively low magma supply rate will turn around and start increasing again in the coming years.

4.4. Implications for eruption forecasting

The decreases in the inflation rate from the waning magma supply have implications for eruption forecasting. Because the eruptions at Axial Seamount appear to be "inflation-predictable" (Nooner and Chadwick, 2016) and there are no negative consequences for false alarms since there are no humans living nearby, we have been experimenting with various methods for extrapolating the rate of inflation into the future to aid in eruption forecasting. The method that currently seems the most robust is to use the *differential* OOI-BPR uplift rate averaged over the previous 6 months to extrapolate into the future (Fig. 11a). From that, we calculate the date that the volcano will reach the level of inflation when the 2015 eruption was triggered, and the date for a level of inflation 20 cm higher (since the 2015 eruption was triggered at a *single-station* level 30 cm higher than the 2011 eruption, and the *differential* inflation values are about 2/3 of the *single-station* values). Using continuous real-time data from the OOI cabled observatory, we make these extrapolations once a day, so they vary with time, depending on the recent inflation rate. Figure 11b shows a histogram of the predicted dates that Axial would reach the 2015 inflation threshold, made daily since the 2015 eruption, and color-coded as a function of time. This shows that as the rate of inflation slowed with time, the predicted date when the volcano would reach the 2015 inflation threshold has moved farther into the future. Another way of showing this is in Figure 11c, in which the predicted date of reaching the 2015 threshold (on the y-axis) is plotted against the date that the prediction was made (on the x-axis). The blue curve is for the 2015 threshold and the purple curve is for an inflation level 20 cm higher. Both Figures 11b and 11c show that the predicted dates were earlier than 2020 from the end of 2015 until mid-2016 when the rate of re-inflation was high. Then as the rate of re-inflation stabilized at a lower level, the predicted dates moved into the

2020-2022 range from mid-2016 to mid-2019. The undulations in the curves in Figure 11c during this interval are due to the short-term deflation events, each of which temporarily moved the predicted dates forward and then back in time. The May 2019 short-term deflation event caused a major perturbation, moving the predicted dates far into the future temporarily (shown by the spike in predicted dates in Fig. 11c), when the inflation rate approached zero. Afterwards, the predicted dates settled down in the 2022-2024 range between mid-2019 to late-2020, due to the lower inflation rate after May 2019. Then after August 2020, the predicted dates moved sharply into the future again as the inflation rate slowed further. Similar plots are updated with the latest OOI-BPR data daily at this URL: https://www.pmel.noaa.gov/eoi/rsn/Forecasts4.html

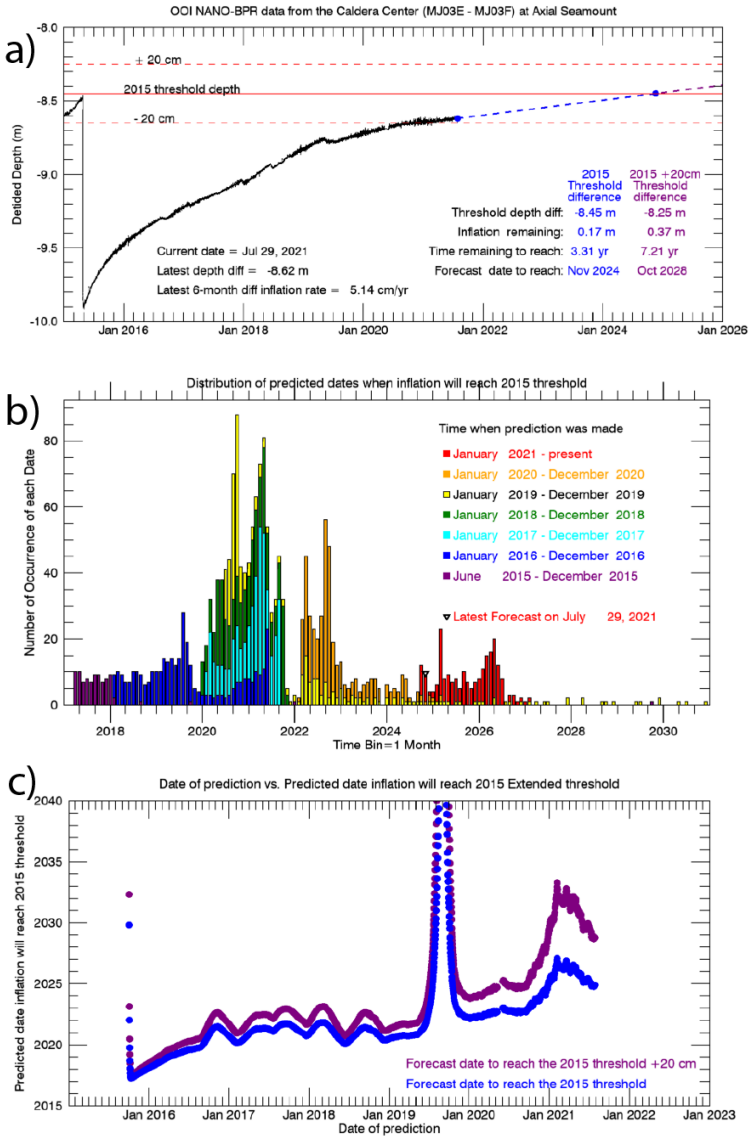

Fig. 11

Figure 11. Inflation threshold forecast plots. (a) Plot of differential BPR data (OOI-BPR-MJ03F-E; black curve) showing re-inflation since the 2015 eruption. A blue dashed line extrapolates into the future using the average rate of inflation from the previous 6 months; blue dot is date when 2015 inflation threshold is reached (see legend). (b) Histogram of predicted dates when inflation will reach the 2015 threshold, color coded by when the predicted date was calculated, based on the average rate of reinflation from the previous 6 months,

beginning in June 2015. Predicted dates are binned in months. (c) Plot of predicted date that inflation will reach the 2015 inflation threshold (Y-axis) vs. date on which the prediction was made (X-axis). Blue dots are date to reach the 2015 inflation threshold; purple dots are for a threshold 20 cm higher. Note predicted dates were earliest when the rate of re-inflation was highest soon after the 2015 eruption (left side of plot). Peaks in the curves show time periods when the average rate of inflation slowed significantly (especially in mid-2019), which pushed the predicted dates farther into the future.

We have used this information to make subjective eruption forecast windows that are periodically revised based on the latest data. In early 2019, when the inflation rate was higher and seemed stable, we created our first post-2015 eruption forecast window between 2020 and 2022 (Chadwick and Nooner, 2019). By late 2019, the slow-down after the May 2019 deflation event was evident, but it was not clear how long it would continue, so we lengthened the eruption forecast window to 2024 (Chadwick et al., 2019). By late 2020, we could see that the slower inflation rate was continuing, so our eruption forecast window was moved further into the future, between 2022 and 2025 (Chadwick et al., 2020). Now (mid-2021), we have widened the forecast window and moved it even further forward to 2025-2035, based on the spread of the latest forecast dates shown in Figure 11c. In addition, we might expect the next eruption to require a somewhat higher inflation threshold (and magmatic pressure), because the historical eruptions at Axial have intruded dikes in both rift zones, and it may take some time for plate spreading to increase the extensional stresses along the rifts again. In any case, because of the real-time geodetic and seismic data available from the OOI-RCA, we can continually adjust the eruption forecast outlook, as rates of inflation and seismicity change. For now, the next eruption appears to be at least 4 years away, consistent with the current relatively low rates of seismicity (Fig. 12a), compared to the rates observed just before the 2015 eruption (Fig. 12b). Therefore, the interval between the 2015 eruption and the next one will likely be more like the 13-year interval between the 1998-2011 eruptions, than the 4-year interval between the 2011-2015 eruptions. A blog of our eruption forecast efforts is kept at this URL: https://www.pmel.noaa.gov/eoi/axial_blog.html.

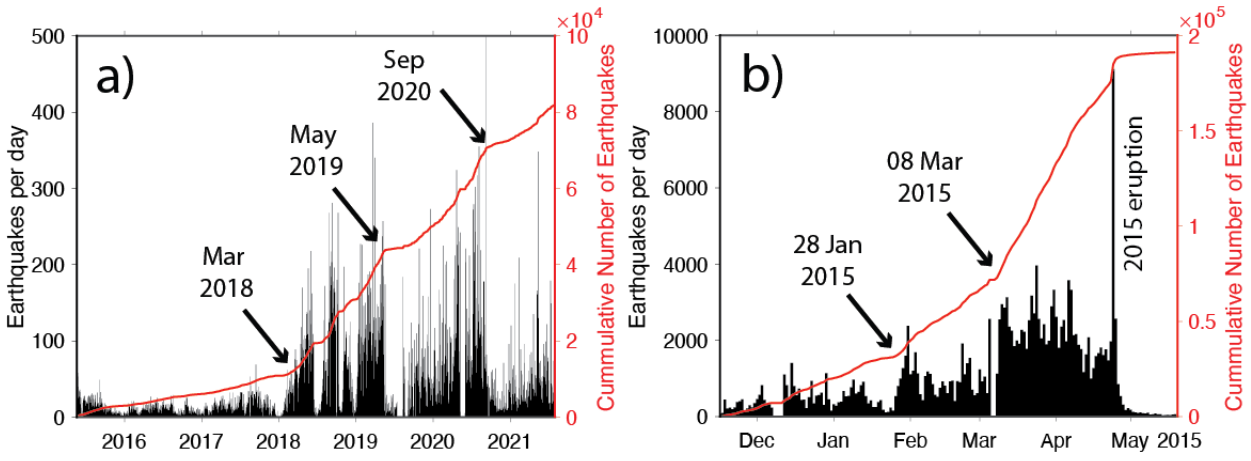

Fig. 12

Figure 12. Histograms of earthquakes per day (black bars) and cumulative number of earthquakes (red curves) over time based on OOI data. (a) Seismicity since the 2015 eruption. (b) Seismicity before the 2015 eruption. Arrows point to times of significant changes in the rate of earthquakes.

4.5. Changes in magma supply at other basaltic volcanoes

The reason that the shallow magma supply at Axial Seamount has varied with time presumably reflects changes in the deep supply from the mantle source region. Similar volcanic settings where continuous inflation data over several decades can be used to quantify a varying magma supply rate are somewhat rare. Kilauea volcano, Hawaii, is one example where variations in magma supply over a period of years have been documented. Poland et al. (2012) showed that the rate of magma supply at Kilauea approximately doubled between 2003-2007, from 0.11 to at least 0.19 km^3/yr, during a time when the volcano was erupting continuously. They interpreted that the surge originated in the mantle and showed how it was manifested at the surface by changes in eruption rate, gas emission, seismicity, and deformation. For example, a short-lived eruption in June 2007 on Kilauea's East Rift Zone erupted high-temperature, high-MgO lava characteristic of freshly supplied magma from the mantle. Similarly, the earliest stages of the 2015 eruption at Axial Seamount also erupted higher-temperature, higher-MgO lava for the first time in 500-600 years, consistent with a surge in the magma supply from the mantle (Chadwick et al., 2016; Clague et al., 2018). While the pre-surge magma supply rate at Axial is about an order of magnitude lower than at Kilauea, the relative magnitude of the surge at Axial was greater than at Kilauea (~10 times larger vs. ~2 times larger), and during Axial's recent surge the magma supply approached Kilauea's background rate. While they both are hotspot volcanoes, their tectonic settings are different, as

Kilauea is in an intraplate setting whereas Axial is superimposed on the axis of a spreading ridge with much thinner oceanic crust.

Another basaltic hotspot volcano near a spreading ridge with a well-documented long-term inflation record and demonstrated variations in magma supply is Sierra Negra volcano in the Galápagos. At Sierra Negra, deformation monitoring since 1992 by InSAR, campaign-GPS, and continuous-GPS shows that inflation rates have varied considerably over several decades. After 8 years of inflation between 1992-1999, several years of little or no inflation followed in 1999-2003, which gave way to a period of rapidly accelerating uplift that led up to the 2005 eruption, eventually approaching a rate of 1 cm/day and a total uplift of ~5 m since 1992 (Chadwick et al., 2006a; Geist et al., 2008). Following 5.4 m of co-eruption deflation in 2005 (Yun et al., 2007), Sierra Negra re-inflated more than 6.5 m before its next eruption in 2018 (Vasconez et al., 2018; Bell et al., 2021a; Bell et al., 2021b). This time, the re-inflation period included five distinct episodes, starting with rapid but decelerating inflation immediately after the 2005 eruption, followed by slower inflation, then several months of minor subsidence in late 2011 and early 2012, then slow inflation again, and ending with a period of a higher inflation rate leading up to the 2018 eruption (Bell et al., 2021a; Bell et al., 2021b). The surface deformation at Sierra Negra is best fit by increase pressure in a sill-like shallow magma reservoir 2 km below the caldera floor (Amelung et al., 2000; Chadwick et al., 2006a; Yun et al., 2006; Jónsson, 2009). However, geobarometric analyses from the 2018 lavas suggest there is a second reservoir at 7.5 km depth (Bell et al., 2021a). Thus, the varying rates of inflation can be interpreted as variations in pressure (and supply) between the shallow and deeper reservoirs (Bell et al., 2021b).

Piton de la Fournaise is another intraplate basaltic hotspot volcano on the island of Reunion in the Indian Ocean where long-term inflation/deflation has been observed over multiple eruption cycles. Peltier et al. (2008) presented monitoring data from a very active period in 2004-2006 that included 6 eruptions. The volcano inflated between some of these eruptions, but at varying rates, and some inflation episodes were separated by periods of minor deflation. The source of the deformation was modeled as a single source at a depth of ~2.3 km below the summit (Peltier et al., 2008). They interpreted these as cycles of magma supply into and out of the shallow reservoir from a deeper reservoir below, with a quasi-continuous (but varying) magma supply. Over a longer time period, a review of monitoring data since 1972 by Peltier et al. (2009) suggests that the magma supply from the mantle has been more intermittent with periods of no significant inflation separating periods of active recharge with multiple eruption cycles, and a more regular supply since 2000.

These examples show that magma supply at oceanic basaltic volcanoes influenced by hotspots can change significantly over time periods of months to years and that such changes (both increases and decreases) are common. With this perspective, the variations we have documented at Axial Seamount are not unusual, and we should perhaps expect to see the magma supply rate increase

again before its next eruption.

4.6. Relationship between deformation and seismicity

Building on the work of Lengliné et al. (2008), Kilburn (2012; 2018) developed a rock-mechanics based physical model to explain how surface uplift and elevated seismicity co-vary with time before eruptions at closed-system caldera-volcanoes. In the model, seismicity and uplift are viewed as proxies for the inelastic and total deformation of a crust, respectively, and the inelastic deformation is accommodated on a dispersed population of small faults. The seismicity and deformation are mutually dependent because they are both controlled by the rate at which the crust is being stressed by magma accumulation, but they evolve differently with time. The model predicts that the rate of seismicity depends on both the uplift rate and the total uplift during an eruption cycle, as a volcano evolves through *elastic*, *quasi-elastic*, and *inelastic* deformation regimes (Kilburn, 2018; Bell et al., 2021b). In the *elastic* and early *quasi-elastic* regimes at the beginning of a cycle, the rate of seismicity is low even though the rate of uplift can be high, because the cumulative deformation and crustal stress state are low (after stress relaxation during the previous eruption). As the total uplift accumulates during re-inflation and differential stresses increase, the model predicts that the number of earthquakes per unit of uplift should increase exponentially with total uplift in the later *quasi-elastic* regime, as small distributed faults become progressively stressed and they begin to accommodate some of the deformation. The seismicity represents the small but growing component of inelastic deformation and damage accumulation in the crust. Once a critical stress threshold is reached, the deformation enters an *inelastic* regime in which most of the deformation is accommodated by brittle failure and fault slip, and both the rate of earthquakes and deformation may increase hyperbolically, leading to failure in the shallow crust between the magma reservoir and the surface, producing an eruption. However, in some cases, a period of constant-rate seismicity and deformation occurs before, or instead of, the hyperbolic phase in the *inelastic* regime (Kilburn, 2018; Bell et al., 2021b).

This elastic-to-brittle physical model has been successfully applied to explain inter-eruption monitoring data at a variety of basaltic caldera volcanoes, including Kilauea, Hawaii (Bell and Kilburn, 2012) and Sierra Negra, Galápagos (Bell et al., 2021b), as well as at silicic calderas with long and complex periods of unrest, such as Rabaul, Papua New Guinea (Robertson and Kilburn, 2016) and Campi Flegrei, Italy (Kilburn et al., 2017). As seen in the previous section, the behavior of Sierra Negra in particular (Bell et al., 2021b) has many parallels to Axial Seamount, and the elastic-to-brittle model appears to fit the observations at both volcanoes quite well. At both volcanoes, there appears to be little or no *elastic* phase and instead an eruption cycle starts right into the *quasi-elastic* phase with seismicity accompanying deformation.

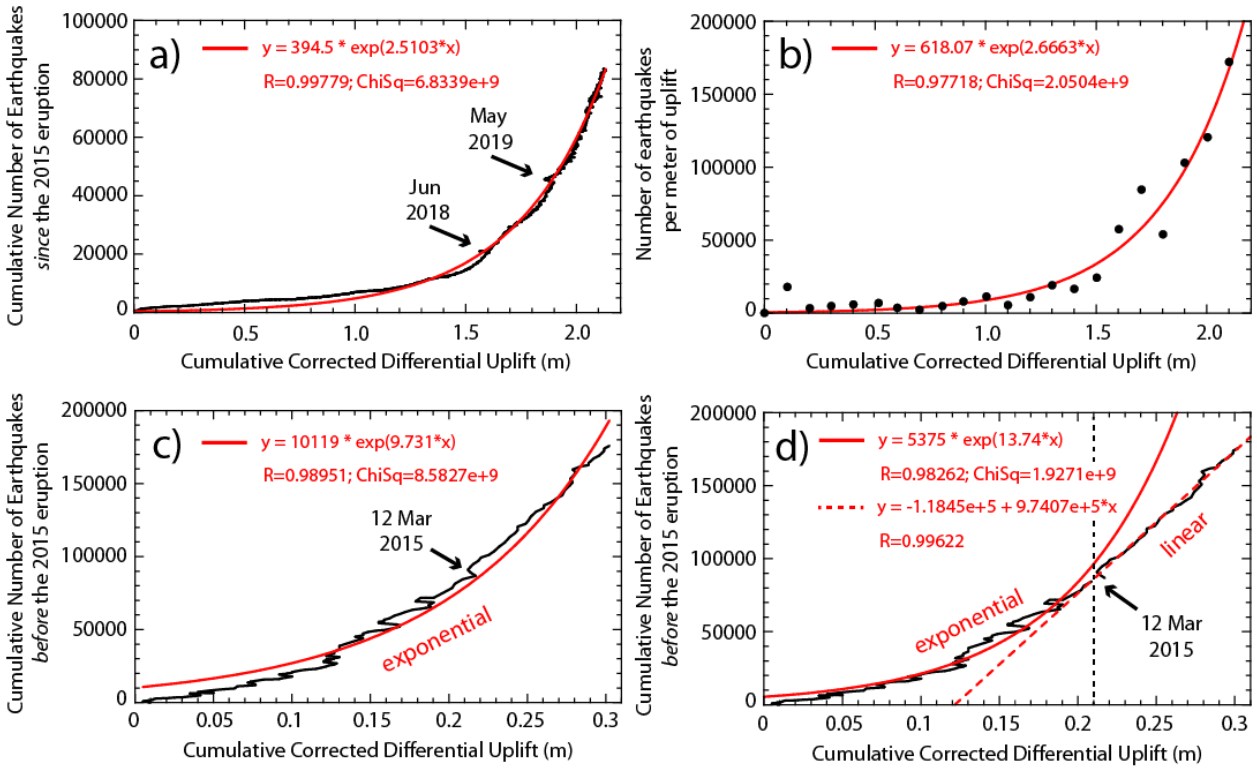

Fig. 13

Figure 13. Plots showing exponential relationship between rates of seismicity and deformation. (a) Black curve is cumulative number of earthquakes vs. total uplift since the 2015 eruption (May 1, 2015 to August 1, 2021). Red curve is best-fitting exponential equation. (b) Earthquake rate per meter of uplift since the 2015 eruption (May 1, 2015 to August 1, 2021), showing that it also follows an exponential relationship (red curve). (c) Cumulative number of earthquakes vs. total uplift *before* the 2015 eruption, starting when the OOI cabled observatory became operational (November 16, 2014 to April 23, 2015). In this plot the data (black curve) are compared to an exponential curve (red curve) over the entire period. (d) Same data as in (c) but separated into two time periods before and after 12 March 2015 (vertical dashed line), and fit to an exponential curve before (solid red line) and to a linear curve after (red dashed line), which could indicate an increasing component of inelastic deformation precursory to the eruption. In all plots, the X-axis is cumulative differential uplift (OOI-BPR-MJ03F-E), corrected to approximate actual uplift at the caldera center by multiplying by 1.67.

Figure 13a shows the cumulative number of earthquakes as a function of total

uplift at Axial Seamount since the 2015 eruption. All of the earthquakes in the Wilcock et al. (2017) catalogue from Axial are considered "volcano-tectonic" or VT, using the terminology in the volcano-seismology literature. In Figure 13a, we use daily averages of the *differential* BPR uplift as the clearest record of volcanic inflation at Axial Seamount, and multiply it by a correction factor of 1.67 to better represent actual *single-station* uplift at the center of the caldera. Most of the earthquakes detected at Axial are between magnitudes 0-2 (the magnitude of completeness is ~0) (Wilcock et al., 2016; Wilcock et al., 2017; Tan et al., 2019) and represent slip on small distributed faults (10-100 m across) consistent with the assumptions in the model of Kilburn (2018). In the first few years after the 2015 eruption, the number of earthquakes per unit uplift was low but it has gradually increased with time and the trend of the cumulative earthquakes to total uplift curve fits an exponential curve rather well (Figure 13a), as predicted by the *quasi-elastic* phase of Kilburn (2018). The increasing number of earthquakes represent an increasing proportion of the deformation being accommodated by inelastic deformation, although the bulk of the deformation remains elastic and slip on the caldera faults is still a minor contributor overall. Another way of showing this is a plot of the number of earthquakes per meter of uplift since the 2015 eruption, which also follows an exponential relationship (Fig. 13b).

At Sierra Negra volcano, Bell et al. (2021b) showed similar relationships between seismicity and deformation between its 2005 and 2018 eruptions. However, in addition they found that in the final 6 months before the 2018 eruption, the number of earthquakes per unit of uplift stopped following an exponential trend and changed to a constant linear trend instead. This was interpreted as the end of the *quasi-elastic* phase and the beginning of the *steady-inelastic* phase of Kilburn (2018), when the differential stress approached a critical failure value (there was no hyperbolic acceleration of seismicity and strain rates before the eruption). We may see a similar pattern before the 2015 eruption at Axial Seamount, but it is less obvious. Figures 13c and 13d show the cumulative number of earthquakes vs. total uplift in the final 5 months before the 2015 eruption at Axial Seamount (note that the totals only reflect the number of earthquakes and the amount of uplift after 16 November 2014, when the seismometers on the OOI cabled observatory became operational). It is ambiguous whether the curve follows an exponential pattern all the way up to the eruption (Fig. 13c), or whether it is exponential until around 12 March 2015 and then becomes linear during the final 1.5 months before the eruption (Fig. 13d). The data can be reasonably fit either way, perhaps because the pre-eruption time period with both seismic and deformation data is limited to only 5 months. Before the next eruption at Axial, it may be more evident whether a shift from exponential to linear occurs, because we will have a complete record of precursory deformation and seismicity over an entire eruption cycle for the first time. At Sierra Negra, Bell et al. (2021b) interpreted that the transition from exponential to linear trends may have signalled the beginning of through-going failure on the trapdoor faults in the caldera floor, perhaps triggering dike

intrusion from the magma reservoir to the surface. At Axial, the seismically active caldera faults could play a similar role either by accumulating enough slip to eventually intersect the shallow magma reservoir, or by triggering dike intrusion from the reservoir and magma ascent to the surface (Cabaniss et al., 2020). Therefore, we will be watching carefully to see if a similar transition from exponential to linear rates in seismicity relative to uplift occurs at Axial during the current eruption cycle, which may signal that the crust surrounding the magma reservoir is becoming critically stressed and is approaching failure.

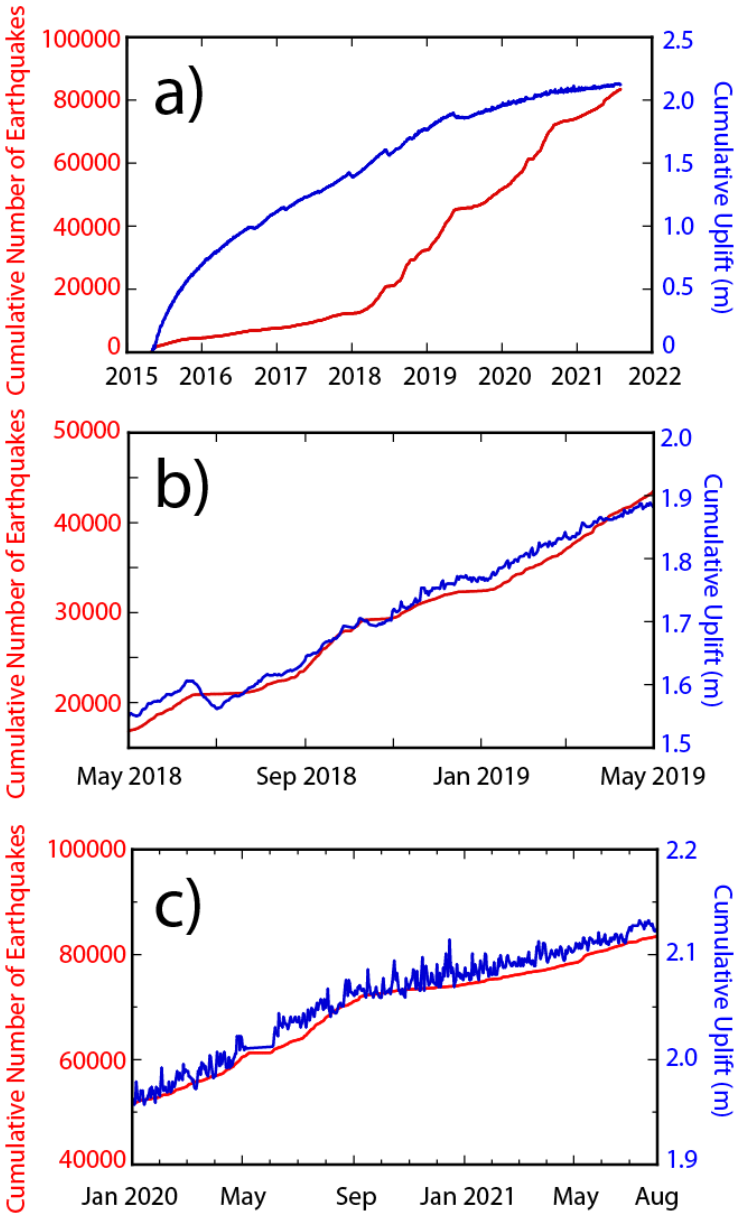

Fig. 14

Figure 14. Plots of the cumulative number of earthquakes and cumulative uplift since the 2015 eruption, showing co-variation over different time periods.

(a) Plot of entire time period (2015 to 2022) shows rate of earthquakes increasing and rate of uplift decreasing, but co-variation of their rates is not obvious. However, over some smaller time periods and with appropriate scaling (b-c), it is clearer that their rates co-vary with coincident rate increases and decreases resulting in cumulative curves that parallel each other. (b) May 2018 to May 2019. (c) January 2020 to August 2021. On the right side of each plot, the blue Y-axis is cumulative differential uplift (OOI-BPR-MJ03F-E), corrected to approximate the single-station uplift at the caldera center by multiplying by 1.67.

The elastic-to-brittle physical model also provides another method to explore for forecasting the timing of the next eruption at Axial Seamount since its precursory pattern appears to be repeatable. The current rate of earthquakes per meter of uplift is ~1.7 x 10^5 m^{-1} (Fig. 13b), which is about 17% of the rate of ~10^6 m^{-1} seen in the 6 weeks prior to the 2015 eruption (Fig. 13d). Assuming a similar threshold for the rate of earthquakes with uplift for the next eruption, the exponential model in Figure 13a would predict that Axial will erupt when the corrected differential uplift reaches ~2.8 m, or ~0.7 m above its current level of ~2.1 m (Fig. 9). Since the 2015 eruption was triggered when the corrected differential uplift was ~2.4 m, that inflation threshold would be ~0.4 m higher than for the 2015 eruption, similar to 0.3 m higher threshold in 2015 compared to 2011. Given that the current rate of inflation is only ~7 cm/yr, this prediction is also consistent with the inference above that the next eruption is still years away at the current rate of inflation.

Bell et al. (2021b) showed that the rate of seismicity at Sierra Negra depends on both total uplift and the uplift rate. The latter was shown by plots of the cumulative uplift and cumulative number of earthquakes over timescales of months to years, highlighting broad changes in the rates of uplift and seismicity that mirrored each other. However, the number of earthquakes per unit of uplift also changes with time, which can obscure the co-variations in rates between the two. For example, Figure 14a shows a plot of the cumulative differential uplift and cumulative number of earthquakes at Axial Seamount with time over the entire post-eruption time period. On first glance, there appears to be little relation between uplift and earthquake rates, because of the long-term decrease in uplift rate and the long-term increase in seismicity. However, if the two are plotted over some shorter time periods (Figs. 14b, c) and scaled appropriately, the co-variation in uplift and earthquake rates becomes more evident. Therefore, not only is seismicity closely linked to deformation during the short-term deflation events, discussed earlier, but in the rest of the re-inflation period as well. This confirms the interpretation that the rates of deformation and seismicity are both controlled by the underlying (and variable) rate of magma accumulation within the shallow reservoir and the cumulative uplift since the last eruption. The growing rate of seismicity represents the growing proportion of inelastic deformation with cumulative uplift.

The model of Kilburn (2018) helps explain how a low rate of seismicity can

accompany a high rate of post-eruption uplift early in Axial's inter-eruption cycle, and yet later in the cycle a lower rate of uplift is associated with a higher rate of seismicity (because the total uplift, accumulated strain and differential stress are all higher). It also successfully predicts that the number of earthquakes per unit of uplift during the inter-eruption period increases exponentially with total uplift. Continued monitoring will show whether pattern recognition and a repeatable critical inflation threshold continues to be an effective way to forecast eruptions at Axial Seamount, or whether changes in the trends of earthquakes per unit of uplift may be a better way to anticipate the timing of failure around the shallow magma reservoir as a precursor to eruption.

5. Conclusions

As of mid-2021, Axial Seamount has re-inflated 85-90% of the deflation it experienced during its last eruption in 2015. However, the long-term rate of inflation has been gradually decreasing since 2015. By using differential BPR data (subtracting data from a reference station to remove oceanographic noise and enhance the geodetic signal), we identified 8 repeated short-term deflation events between August 2016 and May 2019, each associated with a simultaneous drop in seismicity, and some with changes in the average inflation rate. We interpret these as either small movements of magma out of the shallow reservoir or interruptions to the magma supply that may be a consequence of a waning supply from the mantle since the 2015 eruption. The long-term geodetic record suggests that variations in the magma supply rate of about an order of magnitude occur at Axial over decadal time scales, and the current supply rate is ~10 times less than a surge that fed the closely-spaced 2011 and 2015 eruptions. This variation of magma supply from depth over a period of years appears to be common at other basaltic hotspot-influenced volcanoes, and we should anticipate further changes. The decrease in inflation rate since the 2015 eruption has implications for eruption forecasting and our current forecast window is wide and poorly constrained, between 2025-2035, but could change as the rate of inflation continues to vary. This shows that the eruption recurrence interval at Axial strongly depends on the magma supply rate, and that the interval between Axial's last and next eruptions is likely to be closer to the 13 years between 1998-2011, rather than the 4 years between 2011-2015.

The rates of seismicity and deformation since the 2015 eruption at Axial show that they are mutually dependent and co-vary such that the cumulative number of earthquakes increases exponentially with total uplift, due to the increase of differential stress in the crust overlying the shallow magma reservoir caused by magma accumulation. The data are consistent with a physical model of cumulative damage in the crust at volcanoes undergoing inter-eruption re-inflation that increases the component of inelastic deformation with time (the seismicity relative to the total uplift) until a critical threshold is reached that triggers through-going failure between the reservoir and the surface and culminating in an eruption. Extrapolating the current earthquake rates based on the exponential relationship to total uplift and comparison to the 2015 eruption provides

another basis for eruption forecasting. Real-time monitoring data from the OOI cabled observatory at Axial will allow us to compare the effectiveness of eruption forecasts based on the repeating pattern of deformation alone, the exponential model of earthquake rates to total uplift, and recognizing a transition from exponential to linear in the trend of earthquakes to total uplift that may signal imminent failure in the crust over the shallow magma reservoir. In sum, Axial Seamount continues to serve as an outstanding natural laboratory for better understanding the active volcanic processes that lead to eruptions.

Acknowledgements and Data Availability

This paper uses data provided by the Ocean Observatories Initiative, which is a major facility fully funded by the National Science Foundation (NSF). This research was also supported by NSF awards OCE-1356839 and 1736882 to WC and SN, awards OCE-1634150 and 1928282 to WC, and award OCE-1536219 to WW. Additional support was provided by the National Oceanic and Atmospheric Administration, Pacific Marine Environmental Laboratory, Earth-Ocean Interactions Program. We are grateful for the outstanding logistical support at sea provided by the crews of *R/V Thompson* and ROV *Jason*. This work would not have been possible without the hard work of the University of Washington OOI Regional Cabled Array team, led Deborah Kelley and pioneered by John Delaney. The paper benefited from helpful reviews by _____. PMEL contribution #_____.

The data presented here are archived at the NSF Ocean Observatories Initiative Data Portal, http://ooinet.oceanobservatories.org, from Bottom Pressure Tilt instruments (RS03CCAL-MJ03F-BOTPTA301 and RS03ECAL-MJ03E-BOTPTA302), using data from 30 August 2014 to 01 August 2021. Non-cabled pressure datasets are archived at the Marine Geoscience Data System as Chadwick and Nooner (2015) and Fox (2016). The OOI seismic data are archived at the Incorporated Research Institutions for Seismology Data Management System (IRIS), https://www.iris.edu/ and http://fdsn.adc1.iris.edu/networks/detail/OO/. A catalog of seismic data are archived at the Marine Geoscience Data System as Wilcock et al. (2017) and are also available at http://axial.ocean.washington.edu/.

References

Amelung, F., S. Jónsson, H. Zebker, and P. Segall (2000), Widespread uplift and 'trapdoor' faulting on Galápagos volcanoes observed with radar interferometry, Nature, 407, 993-996Arnulf, A. F., A. J. Harding, G. M. Kent, S. M. Carbotte, J. P. Canales, and M. R. Nedimovic (2014), Anatomy of an active submarine volcano, Geology, 42(8), 655-658, doi:10.1130/G35629.1.Arnulf, A. F., A. J. Harding, G. M. Kent, and W. S. D. Wilcock (2018), Structure, seismicity, and accretionary processes at the hotspot-influenced Axial Seamount on the Juan de Fuca Ridge, J. Geophys. Res., 123, doi:10.1029/2017JB015131.Arnulf, A. F., A. Harding, S. Saustrup, A. Kell, G. M. Kent, S. M. Carbotte, J. P. Canales, M. Nedimovic, M. Bellucci, S. Brandt, A. Cap, T. Eischen, M.

Goulain, M. Griffiths, M. Lee, V. Lucas, S. Mitchell, and B. Oller (2019), Imaging the internal workings of Axial Seamount on the Juan de Fuca Ridge. Abstract OS51B-1483 presented at 2019 Fall Meeting, AGU, San Francisco, CA, 9-13 Dec., doi:10.1002/essoar.10504760.1.Arnulf, A. F., S. Saustrup, T. Eischen, A. J. Harding, G. M. Kent, S. M. Carbotte, M. Lee, J. P. Canales, M. Nedimovic, E. Biondi, G. Barnier, B. L. Biondi, and R. G. Clapp (2020), Seismic imaging of the internal workings of Axial Seamount on the Juan de Fuca Ridge. Abstract V043-05 presented at 2020 Fall Meeting, AGU, San Francisco, CA, 7-11 Dec.Baillard, C., W. S. D. Wilcock, A. F. Arnulf, M. Tolstoy, and F. Waldhauser (2019), A joint inversion for three-dimensional P and S wave velocity structure and earthquake locations beneath Axial Seamount, Journal of Geophysical Research: Solid Earth, 124, 12997–13020, doi:10.1029/2019JB017970.Bell, A. F., and C. R. J. Kilburn (2012), Precursors to dyke-fed eruptions at basaltic volcanoes: Insights from patterns of volcano-tectonic seismicity at Kilauea volcano, Hawaii, Bull. Volcanol., 74(2), 325–339, doi:10.1007/s00445-011-0519-3.Bell, A. F., P. C. L. Femina, M. Ruiz, F. Amelung, M. Bagnardi, C. J. Bean, B. Bernard, C. Ebinger, M. Gleeson, J. Grannell, S. Hernandez, M. Higgins, C. Liorzou, P. Lundgren, N. J. Meier, M. Möllhoff, S.-J. Oliva, A. G. Ruiz, and M. J. Stock (2021a), Caldera resurgence during the 2018 eruption of Sierra Negra volcano, Galápagos Islands, Nat Commun, 12(1397), doi:10.1038/s41467-021-21596-4.Bell, A. F., S. Hernandez, P. C. L. Femina, and M. C. Ruiz (2021b), Uplift and seismicity driven by magmatic inflation at Sierra Negra Volcano, Galápagos Islands, Journal of Geophysical Research: Solid Earth, 126, e2021JB022244, doi:10.1029/2021JB022244.Cabaniss, H. E., P. M. Gregg, S. L. Nooner, and W. W. Chadwick Jr. (2020), Triggering of eruptions at Axial Seamount, Juan de Fuca Ridge, Scientific Reports, 10, 10219, doi:10.1038/s41598-020-67043-0.Caplan-Auerbach, J., R. P. Dziak, J. Haxel, D. R. Bohnenstiehl, and C. Garcia (2017), Explosive processes during the 2015 eruption of Axial Seamount, as recorded by seafloor hydrophones, Geochem. Geophys. Geosyst., 18, 1761-1774, doi:10.1002/ 2016GC006734.Carbotte, S. M., A. F. Arnulf, M. W. Spiegelman, M. Lee, A. J. Harding, G. M. Kent, J. P. Canales, and M. R. Nedimović (2020), Stacked sills forming a deep melt-mush feeder conduit beneath Axial Seamount, Geology, 48, doi:10.1130/G47223.1.Caress, D. W., D. A. Clague, J. B. Paduan, J. Martin, B. Dreyer, W. W. Chadwick, Jr., A. Denny, and D. S. Kelley (2012), Repeat bathymetric surveys at 1-metre resolution of lava flows erupted at Axial Seamount in April 2011, Nature Geosci., 5(7), 483-488, doi:10.1038/NGEO1496.Caress, D. W., D. A. Clague, J. B. Paduan, H. Thomas, W. W. Chadwick, Jr., S. L. Nooner, and D. R. Yoerger (2015), Vertical deformation of the Axial Seamount summit from repeated 1-m scale bathymetry surveys with AUVs. Abstract presented at 2015 Annual GSA Meeting, Baltimore, MD, 1-4 Nov., GSA Abstracts with Programs, 47(7)Caress, D. W., D. A. Clague, J. B. Paduan, H. J. Thomas, W. W. Chadwick, Jr., S. L. Nooner, and D. R. Yoerger (2016), Vertical deformation of the Axial Seamount summit from repeated 1-m scale bathymetry surveys using AUVs. Abstract OS41C-1991 presented at 2016 Fall Meeting, AGU, San Francisco,

Calif., 12-16 Dec.Caress, D. W., D. A. Clague, J. B. Paduan, W. W. Chadwick, Jr., S. L. Nooner, and H. J. Thomas (2020), Vertical Deformation of the Axial Seamount Summit from Repeated 1-m Scale Bathymetry Surveys Using AUVs. Abstract V040-0017 presented at 2020 Fall Meeting, AGU, San Francisco, CA, 7-11 Dec.Chadwick, J., M. Perfit, I. Ridley, I. Jonasson, G. Kamenov, W. W. Chadwick, Jr., R. Embley, P. Le Roux, and M. Smith (2005), Magmatic effects of the Cobb Hotspot on the Juan de Fuca Ridge, Journal of Geophysical Research: Solid Earth, 110, B03101, doi:10.1029/2003JB002767.Chadwick, W. W., Jr., D. J. Geist, S. Jónsson, M. Poland, D. J. Johnson, and C. M. Meertens (2006a), A volcano bursting at the seams: Inflation, faulting, and eruption at Sierra Negra Volcano, Galápagos, Geology, 34(12), 1025-1028, doi: 10.1130/G22826A.1.Chadwick, W. W., Jr., S. Nooner, M. Zumberge, R. W. Embley, and C. G. Fox (2006b), Vertical deformation monitoring at Axial Seamount since its 1998 eruption using deep-sea pressure sensors, J. Volcanol. Geotherm. Res., 150, 313-327, doi:10.1016/j.jvolgeores.2005.07.006.Chadwick, W. W., Jr., S. L. Nooner, D. A. Butterfield, and M. D. Lilley (2012), Seafloor deformation and forecasts of the April 2011 eruption at Axial Seamount, Nature Geosci., 5(7), 474-477, doi:10.1038/NGEO1464.Chadwick, W. W., Jr., D. A. Clague, R. W. Embley, M. R. Perfit, D. A. Butterfield, D. W. Caress, J. B. Paduan, J. F. Martin, P. Sasnett, S. G. Merle, and A. M. Bobbitt (2013), The 1998 eruption of Axial Seamount: New Insights on submarine lava flow emplacement from high-resolution mapping, Geochemistry, Geophysics, and Geosystems, 14(10), 3939-3968, doi:10.1002/ggge.20202.Chadwick, W. W., Jr., and S. L. Nooner (2015), Processed Bottom Pressure Recorder (BPR) data from uncabled instruments deployed at Axial Seamount on the Juan de Fuca Ridge (investigators William Chadwick and Scott Nooner). Integrated Earth Data Applications (IEDA). http://doi.org/10.1594/IEDA/322282Chadwick, W. W., Jr., B. P. Paduan, D. A. Clague, B. M. Dreyer, S. G. Merle, A. M. Bobbitt, D. W. Caress, B. Philip, D. S. Kelley, and S. L. Nooner (2016), Voluminous eruption from a zoned magma body after an increase in supply rate at Axial Seamount, Geophys. Res. Lett., 43, 12063-12070, doi:10.1002/2016GL071327.Chadwick, W. W., Jr., and S. L. Nooner (2019), Forecasting Eruptions Based on an Inflation-Predictable Pattern of Deformation at Axial Seamount, NE Pacific Ocean. Abstract presented at 2019 IUGG General Assembly, Montreal, Canada, 8-18 Jul.Chadwick, W. W., Jr., S. L. Nooner, and T.-K. Lau (2019), Forecasting the Next Eruption at Axial Seamount Based on an Inflation-Predictable Pattern of Deformation. Abstract OS51B-1489 presented at 2019 Fall Meeting, AGU, San Francisco, CA, 9-13 Dec., doi:10.1002/essoar.10504760.1.Chadwick, W. W., Jr., S. L. Nooner, W. S. D. Wilcock, S. M. Carbotte, J. W. Beeson, A. M. Sawyer, and E. K. Fredrickson (2020), Repeated short-term deflation events observed during long-term inflation at Axial Seamount. Abstract V043-06 presented at 2020 Fall Meeting, AGU, San Francisco, CA, 7-11 Dec.Clague, D. A., J. B. Paduan, D. W. Caress, W. W. Chadwick Jr., M. L. Saout, B. Dreyer, and R. Portner (2017), High-resolution AUV mapping and targeted ROV observations of three historical lava flows at Axial Seamount, Oceanography, 30(4), 82-99,

doi:10.5670/oceanog.2017.426.Clague, D. A., J. B. Paduan, B. M. Dreyer, W. W. Chadwick Jr., K. R. Rubin, M. R. Perfit, and A. T. Fundis (2018), Chemical variations in the 1998, 2011, and 2015 lava flows from Axial Seamount, Juan de Fuca Ridge: Cooling during ascent, lateral transport, and flow, Geochem. Geophys. Geosyst., 19, 2915-2933, doi:10.1029/2018GC007708.Cook, M. J., G. S. Sasagawa, and M. A. Zumberge (2019), Drift Corrected Pressure Time Series at Axial Seamount, July 2018 to Present. Abstract OS51B-1488 presented at 2019 Fall Meeting, AGU, San Francisco, CA, 9-13 Dec.Dobashi, Y., and D. Inazu (2021), Improving Detectability of Seafloor Deformation From Bottom Pressure Observations Using Numerical Ocean Models, Front. Ear. Sci., 8(598270), doi:10.3389/feart.2020.598270.Dziak, R. P., and C. G. Fox (1999), Long-term seismicity and ground deformation at Axial Volcano, Juan de Fuca Ridge, Geophys. Res. Lett., 26(24), 3641-3644Dziak, R. P., J. H. Haxel, D. R. Bohnenstiehl, W. W. Chadwick, Jr., S. L. Nooner, M. J. Fowler, H. Matsumoto, and D. A. Butterfield (2012), Seismic precursors and magma ascent before the April 2011 eruption at Axial Seamount, Nature Geosci., 5(7), 478-482, doi:10.1038/NGEO1490.Embley, R. W., K. M. Murphy, and C. G. Fox (1990), High resolution studies of the summit of Axial Volcano, J. Geophys. Res., 95, 12785-12812Embley, R. W., W. W. Chadwick, Jr., D. Clague, and D. Stakes (1999), The 1998 Eruption of Axial Volcano: Multibeam anomalies and seafloor observations, Geophys. Res. Lett., 26(23), 3425-2428, doi:10.1029/1999GL002328.Fox, C. G. (1990), Evidence of active ground deformation on the mid-ocean ridge: Axial Seamount, Juan de Fuca Ridge, April-June, 1988, J. Geophys. Res., 95, 12813-12822Fox, C. G. (1993), Five years of ground deformation monitoring on Axial Seamount using a bottom pressure recorder, Geophys. Res. Lett., 20(17), 1859-1862Fox, C. G. (1999), In situ ground deformation measurements from the summit of Axial Volcano during the 1998 volcanic episode, Geophys. Res. Lett., 26(23), 3437-3440Fox, C. G. (2016), Processed Bottom Pressure Recorder (BPR) data from uncabled instruments deployed at Axial Seamount on the Juan de Fuca Ridge (investigator Chris Fox). Integrated Earth Data Applications (IEDA). http://dx.doi.org/10.1594/IEDA/322344Fredrickson, E. K., W. S. D. Wilcock, D. A. Schmidt, P. MacCready, E. Roland, A. L. Kurapov, M. A. Zumberge, and G. S. Sasagawa (2019), Optimizing sensor configurations for the detection of slow-slip earthquakes in seafloor pressure records, using the Cascadia Subduction Zone as a case study, Journal of Geophysical Research: Solid Earth, 124, doi:10.1029/2019JB018053.Geist, D. J., K. S. Harpp, T. R. Naumann, M. Poland, W. W. Chadwick, Jr., M. Hall, and E. Rader (2008), The 2005 eruption of Sierra Negra volcano, Galápagos, Ecuador, Bull. Volcanol., 70(6), 655-673, doi:10.1007/s00445-007-0160-3.Hefner, W., S. L. Nooner, W. W. Chadwick, Jr., and D. W. R. Bohnenstiehl (2020), Revised magmatic source models for the 2015 eruption at Axial Seamount including estimates of fault-induced deformation, Journal of Geophysical Research: Solid Earth, 125(4), e2020JB019356, doi:10.1029/2020JB019356.Inazu, D., R. Hino, and H. Fujimoto (2012), A global barotropic ocean model driven by synoptic atmospheric disturbances for detecting seafloor vertical displacements

from in situ ocean bottom pressure measurements, Mar. Geophys. Res., doi:10.1007/s11001-012-9151-7.Jónsson, S. (2009), Stress interaction between magma accumulation and trapdoor faulting on Sierra Negra Volcano, Galápagos, Tectonophysics, 471(1-2), 36-44, doi: 10.1016/j.tecto.2008.08.005.Kelley, D. S., J. R. Delaney, and S. K. Juniper (2014), Establishing a new era of submarine volcanic observatories: Cabling Axial Seamount and the Endeavour Segment of the Juan de Fuca Ridge, Mar. Geol., 352, 426-450, doi:10.1016/j.margeo.2014.03.010.Kilburn, C. (2012), Precursory deformation and fracture before brittle rock failure and potential application to volcanic unrest, J. Geophys. Res., 117, B02211, doi:02210.01029/02011JB008703Kilburn, C. R. J., G. De Natale, and S. Carlino (2017), Progressive approach to eruption at Campi Flegrei caldera in southern Italy, Nat Commun, 8:15312, doi:10.1038/ncomms15312.Kilburn, C. R. J. (2018), Forecasting Volcanic Eruptions: Beyond the Failure Forecast Method, Front. Ear. Sci., 6:133, doi:10.3389/feart.2018.00133.Le Saout, M., D. R. Bohnenstiehl, J. B. Paduan, and D. A. Clague (2020), Quantification of eruption dynamics on the north rift at Axial Seamount, Juan de Fuca Ridge, Geochem. Geophys. Geosyst., 21, e2020GC009136, doi:10.1029/2020GC009136.Lengliné, O., D. Marsan, J.-L. Got, V. Pinel, V. Ferrazzini, and P. G. Okubo (2008), Seismicity and deformation induced by magma accumulation at three basaltic volcanoes, J. Geophys. Res., 113, B12305, doi:12310.11029/12008JB005937Levy, S., D. R. Bohnenstiehl, P. Sprinkle, M. S. Boettcher, W. S. D. Wilcock, M. Tolstoy, and F. Waldhauser (2018), Mechanics of fault reactivation before, during, and after the 2015 eruption of Axial Seamount, Geology, doi:10.1130/G39978.1.Manalang, D., W. S. D. Wilcock, G. Cram, J. Tilley, M. Harrington, and D. Martin (2019), Testing the A-0-A Approach to Pressure Gauge Calibrations on Cabled Observatories. Abstract S33D-0616 presented at 2019 Fall Meeting, AGU, San Francisco, CA, 9-13 Dec.Muramoto, T., Y. Ito, D. Inazu, L. M. Wallace, R. Hino, S. Suzuki, S. C. Webb, and S. Henrys (2019), Seafloor crustal deformation on ocean bottom pressure records with non tidal variability corrections: application to Hikurangi margin, New Zealand, Geophys. Res. Lett., 46(1), 303-310, doi:10.1029/2018GL080830.Natalie, J., D. C. Soule, T. J. Crone, W. W. Chadwick, Jr., and W. S. D. Wilcock (2018), The relationship between post-2015 eruption deformation and seismicity rates since the 2015 eruption at Axial Seamount using OOI data. Abstract V43G-0211 presented at 2018 Fall Meeting, AGU, Washington, DC, 10-14 Dec.Nooner, S. L., and W. W. Chadwick, Jr. (2009), Volcanic inflation measured in the caldera of Axial Seamount: Implications for magma supply and future eruptions, Geochem. Geophys. Geosyst., 10, Q02002, doi:10.1029/2008GC002315.Nooner, S. L., and W. W. Chadwick, Jr. (2016), Inflation-predictable behavior and co-eruption deformation at Axial Seamount, Science, 354(6318), 1399-1403, doi:10.1126/science.aah4666.Nooner, S. L., W. W. Chadwick, Jr., D. W. Caress, J. B. Paduan, and D. A. Clague (2017), Using high-resolution repeat AUV bathymetry to constrain magma dynamics at Axial Seamount. Abstract presented at IAVCEI 2017 General Assembly, 14-18 August, Portland, Oregon, USAPeltier, A., V. Famin, P. Bachèlery, V. Cayol, Y. Fukushima, and T. Stau-

dacher (2008), Cyclic magma storages and transfers at Piton de La Fournaise volcano (La Réunion hotspot) inferred from deformation and geochemical data, Earth Planet. Sci. Lett., 270(3-4), 180-188Peltier, A., P. Bachèlery, and T. Staudacher (2009), Magma transfer and storage at Piton de La Fournaise (La Réunion Island) between 1972 and 2007: a review of geophysical and geochemical data, J. Volcanol. Geotherm. Res., 184(1-2), 93-108Poland, M., A. Miklius, A. J. Sutton, and C. R. Thornber (2012), A mantle-driven surge in magma supply to Kilauea Volcano during 2003-2007, Nature Geosci., 5, 295-300, doi:10.1038/ngeo1426.Polster, A., M. Fabian, and H. Villinger (2009), Effective resolution and drift of Paroscientific pressure sensors derived from long-term seafloor measurements, Geochem. Geophys. Geosyst., 10(8), Q08008, doi:10.1029/2009GC002532.Robertson, R. M., and C. R. J. Kilburn (2016), Deformation regime and long-term precursors to eruption at large calderas: Rabaul, Papua New Guinea, Earth Planet. Sci. Lett., 438, 86-94, doi:10.1016/j.epsl.2016.01.003.Roche, O., T. H. Druitt, and O. Merle (2000), Experimental study of caldera formation, J. Geophys. Res., 105(B1), 395-416Sasagawa, G. S., M. J. Cook, and M. A. Zumberge (2016), Drift-corrected seafloor pressure observations of vertical deformation at Axial Seamount 2013–2014, Earth and Space Science, 3, doi:10.1002/2016EA000190.Sawyer, A. M., S. L. Nooner, W. W. Chadwick, Jr., and T.-K. Lau (2019), Short-term fluctuations in magma supply rate and magma dynamics at Axial Seamount. Abstract OS51B-1487 presented at 2019 Fall Meeting, AGU, San Francisco, CA, 9-13 Dec.Sawyer, A. M. (2020), Short-term fluctuations in magma supply at Axial Seamount, Juan de Fuca Ridge, Masters Thesis, 76 pp, University of North Carolina at Wilmington.Sohn, R. A., S. C. Webb, and W. C. Crawford (1999), Local seismicity following the 1998 eruption of Axial Volcano, Geophys. Res. Lett., 26(23), 3433-3436Sohn, R. A., A. H. Barclay, and S. C. Webb (2004), Microearthquake patterns following the 1998 eruption of Axial Volcano, Juan de Fuca Ridge: Mechanical relaxation and thermal strain, J. Geophys. Res., 109(B1), B01101, doi: 01110.01029/02003JB002499Tan, Y. J., F. Waldhauser, M. Tolstoy, and W. S. D. Wilcock (2019), Axial Seamount: Periodic tidal loading reveals stress dependence of the earthquake size distribution (b value), Earth Planet. Sci. Lett., 512, 39–45Vasconez, F., P. Ramón, S. Hernandez, S. Hidalgo, B. Bernard, M. Ruiz, A. Alvarado, P. L. Femina, and G. Ruiz (2018), The different characteristics of the recent eruptions of Fernandina and Sierra Negra volcanoes (Galápagos, Ecuador), Volcanica, 1(2), 127-133, doi:10.30909/vol.01.02.127133 Waldhauser, F., W. S. D. Wilcock, M. Tolstoy, C. Baillard, Y. J. Tan, and D. P. Schaff (2020), Precision seismic monitoring and analysis at Axial Seamount using a real-time double-difference system, Journal of Geophysical Research: Solid Earth, 125, e2019JB018796, doi:10.1029/2019JB018796.Wallace, L. M., S. C. Webb, Y. Ito, K. Mochizuki, R. Hino, S. Henrys, S. Y. Schwartz, and A. F. Sheehan (2016), Slow slip near the trench at the Hikurangi subduction zone, New Zealand, Science, 352(6286), 701-704, doi:10.1126/science.aaf2349.West, M. E., W. Menke, M. Tolstoy, S. Webb, and R. Sohn (2001), Magma storage beneath Axial Volcano on the Juan de Fuca mid-ocean ridge, Nature, 413, 833-836Wilcock, W. S.

D., M. Tolstoy, F. Waldhauser, C. Garcia, Y. J. Tan, D. R. Bohnenstiehl, J. Caplan-Auerbach, R. P. Dziak, A. F. Arnulf, and M. E. Mann (2016), Seismic constraints on caldera dynamics from the 2015 Axial Seamount eruption, Science, 354(6318), 1395-1399, doi:10.1126/science.aah5563.Wilcock, W. S. D., F. Waldhauser, and M. Tolstoy (2017), Catalogs of earthquake recorded on Axial Seamount from January, 2015 through November, 2015 (investigators William Wilcock, Maya Tolstoy, Felix Waldhauser). Interdisciplinary Earth Data Alliance. https://doi.org/10.1594/IEDA/323843Wilcock, W. S. D., R. P. Dziak, M. Tolstoy, W. W. Chadwick Jr., S. L. Nooner, D. R. Bohnenstiehl, J. Caplan-Auerbach, F. Waldhauser, A. Arnulf, C. Baillard, T.-K. Lau, J. H. Haxel, Y. J. Tan, C. Garcia, S. Levy, and M. E. Mann (2018), The recent volcanic history of Axial Seamount: Geophysical insights into past eruption dynamics with an eye toward enhanced observations of future eruptions, Oceanography, 31(1), 114-123, doi:10.5670/oceanog.2018.117.Wilcock, W. S. D., D. A. Manalang, E. K. Fredrickson, M. J. Harrington, G. Cram, J. Tilley, J. Burnett, D. Martin, T. Kobayashi, and J. M. Paros (2021), A Thirty-Month Seafloor Test of the A-0-A Method for Calibrating Pressure Gauges, Front. Ear. Sci., 8, 600671, doi:10.3389/feart.2020.600671.Xu, G., W. W. Chadwick Jr., W. S. D. Wilcock, K. G. Bemis, and J. R. Delaney (2018), Observation and Modeling of Hydrothermal Response to the 2015 Eruption at Axial Seamount, Northeast Pacific, Geochem. Geophys. Geosyst., 19, 2780-2797, doi:10.1029/2018GC007607.Yun, S.-H., P. Segall, and H. A. Zebker (2006), Constraints on Magma Chamber Geometry at Sierra Negra Volcano, Galápagos Islands, based on InSAR Observations, J. Volcanol. Geotherm. Res., 150, 232-243, doi:10.1016/j.jvolgeores.2005.07.009.Yun, S.-H., H. A. Zebker, P. Segall, A. Hooper, and M. Poland (2007), Interferogram formation in the presence of complex and large deformation, Geophys. Res. Lett., 34, L12305, doi:12310.11029/12007GL029745

Table 1. Axial Seamount short-term deflation events identified since the 2015 eruption

Short-term Deflation Event ID	Start o
Aug 2016	24-Aug
Feb 2017	5-Feb-2
Jul 2017	20-Jul-
Dec 2017	18-Dec
Jun 2018	14-Jun
Oct 2018	8-Oct-2
Dec 2018	19-Dec
May 2019	10-May

* Start of reinflation for the May 2019 deflation event wasn't until 22-Jul-2019, ~2 months after deflation stopped.